NASA Technical Memorandum 104566, Vol. 41

SeaWiFS Technical Report Series

Stanford B. Hooker and Elaine R. Firestone, Editors

Volume 41, Case Studies for SeaWiFS Calibration and Validation, Part 4

Eueng-nan Yeh, Robert A. Barnes, Michael Darzi, Lakshmi Kumar,
Edward A. Early, B. Carol Johnson, James L. Mueller, and Charles C. Trees

August 1997

NASA Technical Memorandum 104566, Vol. 41

SeaWiFS Technical Report Series

Stanford B. Hooker, Editor
NASA Goddard Space Flight Center, Greenbelt, Maryland

Elaine R. Firestone, Technical Editor
General Sciences Corporation, Laurel, Maryland

Volume 41, Case Studies for SeaWiFS Calibration and Validation, Part 4

Eueng-nan Yeh, Robert A. Barnes, and Michael Darzi
General Sciences Corporation, Laurel, Maryland

Lakshmi Kumar
Hughes STX, Landover, Maryland

Edward A. Early and B. Carol Johnson
National Institute of Standards and Technology, Gaithersburg, Maryland

James L. Mueller and Charles C. Trees
Center for Hydro-Optics and Remote Sensing/SDSU, San Diego, California

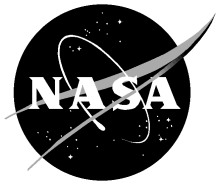

National Aeronautics and
Space Administration

Goddard Space Flight Center
Greenbelt, Maryland 20771

1997

Preface

The scope of the Sea-viewing Wide Field-of-view Sensor (SeaWiFS) Calibration and Validation Program encompasses a broad variety of topics, as evidenced by the contents of three previous *case studies* volumes in the *SeaWiFS Technical Report Series*—Volumes 13, 19, and 27. Each case studies volume contains several chapters discussing topics germane to the Calibration and Validation Program. Volume 41, the fourth collection of case studies, further demonstrates both the breadth and complexity of the issues that the Program must address, and provides further justification for a comprehensive calibration and validation effort.

The chapters in this volume present discussions of the:

a) Calibration and characterization of the GSFC sphere;

b) Revised SeaWiFS algorithm for the diffuse attenuation coefficient $K(490)$;

c) Simplified out-of-band correction algorithm for SeaWiFS; and

d) Stray light correction algorithm implementation.

Greenbelt, Maryland — C. R. McClain
June 1997

Table of Contents

Prologue **1**
1. Calibration and Characterization of the GSFC Sphere **3**
1.1 Introduction **3**
1.2 Aperture Uniformity **4**
1.3 Spectral Radiance **11**
1.3.1 Experimental Procedures **11**
1.3.2 Results **13**
1.4 Ancillary SXR Measurements **15**
1.5 Conclusions **17**
2. Revised SeaWiFS Algorithm for the Diffuse Attenuation Coefficient $K(490)$ **18**
2.1 Introduction **18**
2.2 Data and Methods **19**
2.3 Results **19**
2.4 Discussion **21**
3. Simplified Out-of-Band Correction Algorithm for SeaWiFS **22**
3.1 Introduction **22**
3.2 The `out_bandsub` Algorithm **22**
4. SeaWiFS Stray Light Correction Algorithm **24**
4.1 Introduction **24**
4.2 LAC Correction **24**
4.3 GAC Correction **30**
4.4 Stray Light Masking **30**
Glossary **31**
Symbols **31**
References **32**
The SeaWiFS Technical Report Series **33**

Abstract

This document provides brief reports, or case studies, on a number of investigations sponsored by the Calibration and Validation Team (CVT) within the Sea-viewing Wide Field-of-view Sensor (SeaWiFS) Project. Chapter 1 describes the calibration and characterization of the GSFC sphere, which was used in the recent recalibration of the SeaWiFS instrument. Chapter 2 presents a revision of the diffuse attenuation coefficient, $K(490)$, algorithm based on the SeaWiFS wavelengths. Chapter 3 provides an implementation scheme for an algorithm to remove out-of-band radiance when using a sensor calibration based on a finite width (truncated) spectral response function, e.g., between the 1% transmission points. Chapter 4 describes the implementation schemes for the stray light quality flag (local area coverage [LAC] and global area coverage [GAC]) and the LAC stray light correction.

Prologue

The purposes of the Sea-viewing Wide Field-of-view Sensor (SeaWiFS) Project is to obtain valid ocean color data of the world ocean for a five-year period, to process that data in conjunction with ancillary data to meaningful biological parameters, and to make that data readily available to researchers. The National Aeronautics and Space Administration (NASA) Goddard Space Flight Center (GSFC) will develop a data processing and archiving system in conjunction with the Earth Observing System Data and Information System (EOSDIS), which includes a ground receiving system. In addition, the SeaWiFS Project will oversee a calibration and validation effort which is designed to ensure the integrity of the final products.

The Calibration and Validation Team (CVT) has three main tasks:

1) Calibration and characterization of the SeaWiFS instrument;
2) Development and validation of the operational atmospheric correction algorithm; and
3) Development and validation of the derived product algorithms, such as chlorophyll *a* concentration.

Some of this work will be done internally at GSFC, while the remainder will be done externally at other institutions. NASA and the Project place the highest priority on ensuring the accuracy of derived water-leaving radiances globally, and over the duration of the entire mission. If these criteria are met, the development of global and regional biogeochemical algorithms can proceed on many fronts. These various activities are discussed in detail in *The SeaWiFS Calibration and Validation Plan* (McClain et al. 1992).

Because many of the studies and other works undertaken with the Calibration and Validation Program are not extensive enough to require dedicated volumes of the *SeaWiFS Technical Report Series*, the CVT has decided to publish volumes composed of brief, but topically specific, chapters. Volume 13 is the first volume, and consists primarily of contributions related to atmospheric correction methodologies, ancillary data sets required for level-2 processing of Coastal Zone Color Scanner (CZCS) and SeaWiFS data, laboratory techniques for instrument calibration relevant to calibration round-robins, and field observations designed for transferring the prelaunch calibration to orbit, and in interpreting the on-orbit lunar calibration data. The second case studies volume, Volume 19, contains chapters on atmospheric and glint corrections; solar-, lunar-, and integrating sphere optical measurements; data format considerations; and the use of ancillary data (including surface wind velocities) in SeaWiFS processing. Volume 27 is the third in the set of such volumes and contains chapters on measuring immersion coefficients, oxygen absorption, solar calibration experiments, ship shadow effects on radiance and irradiance measurements, and the definition of the SeaWiFS data day for level-3 data binning. Volume 41 is the fourth of the case studies volumes. A short synopsis of each chapter in this volume is given below.

1. Calibration and Characterization of the GSFC Sphere

A large integrating sphere source, which is owned and maintained by the Sensor Development and Calibration Branch at GSFC, was calibrated and characterized by the Optical Technology Division at the National Institute of Standards and Technology (NIST). This effort, in support of the GSFC SeaWiFS Project, is part of an interagency agreement between NASA and NIST. The spectral radiance was measured for four different lamp settings of the sphere source from 370–1,100 nm every 10 nm using a NIST standard tungsten strip lamp and a prism-grating monochromator which was equipped with a silicon photodiode. The results are presented as a function of wavelength with a relative standard uncertainty of 0.29–2.6% (k=1), depending on the measurement conditions. During these measurements, the SeaWiFS Transfer Radiometer (SXR) was used to determine the spectral radiance of the sphere source at six fixed wavelengths. In

a separate study, the SXR was used to measure the spatial uniformity of the spectral radiance at the exit port of the sphere source. The measurements were made at three wavelengths and at the same four lamp settings for the sphere. The radiance in the aperture was found to be uniform to within 0.6–2.2% (peak-to-valley variability), depending on the measurement conditions. This study was motivated by the requirement that the sphere source perform post-environmental calibrations of the SeaWiFS instrument, as well as to compare the various radiometric scales in use by the ocean color community which are all NIST traceable. The measurements in this report were made just before the fourth SeaWiFS Intercalibration Round-Robin Experiment (SIRREX-4).

2. *Revised SeaWiFS Prelaunch Algorithm for the Diffuse Attenuation Coefficient K(490)*

The algorithm relating the diffuse attenuation coefficient $K(490)$ at 490 nm to the ratio of water-leaving radiances $L_W(443)/L_W(555)$ is evaluated through regression analysis of radiometric profiles from oceanographic cruises in the Arabian Sea, Sargasso Sea, the California Current System, the Gulf of California, and the North and South Atlantic Oceans. The resulting algorithm coefficients for this wavelength combination are significantly different, at the 95% confidence level, from those of the CZCS $K(490)$ algorithm based on the ratio $L_W(443)/L_W(550)$. It is recommended, therefore, that the coefficients from the present analysis, rather than those of the CZCS algorithm, be used for the prelaunch SeaWiFS $K(490)$ algorithm.

3. *A Simplified Out-of-Band Correction Algorithm for SeaWiFS*

The SeaWiFS instrument will scan through a broad area of known radiance, and the measurement for each band may contain signals from outside the desired bandwidth. A calculation that will quickly remove the out-of-band contamination is presented in this chapter.

4. *SeaWiFS Stray Light Correction Algorithm*

SeaWiFS will scan through not only the dark ocean surface, but also the bright land, clouds, and ice objects. Because of stray light in the SeaWiFS instrument, light from these bright sources can contaminate ocean measurements several pixels away from a bright source. A mathematical formula that can be used to correct this contamination is discussed in this section.

Chapter 1

Calibration and Characterization of the GSFC Sphere

Edward A. Early and B. Carol Johnson
National Institute of Standards and Technology
Gaithersburg, Maryland

Abstract

A large integrating sphere source, which is owned and maintained by the Sensor Development and Calibration Branch at GSFC, was calibrated and characterized by the Optical Technology Division at NIST. This effort, in support of the GSFC SeaWiFS Project, is part of an interagency agreement between NASA and NIST. The spectral radiance was measured for four different lamp settings of the sphere source from 370–1,100 nm every 10 nm using a NIST standard tungsten strip lamp and a prism-grating monochromator which was equipped with a silicon photodiode. The results are presented as a function of wavelength with a relative standard uncertainty of 0.29–2.6% (k=1), depending on the measurement conditions. During these measurements, the SXR was used to determine the spectral radiance of the sphere source at six fixed wavelengths. In a separate study, the SXR was used to measure the spatial uniformity of the spectral radiance at the exit port of the sphere source. The measurements were made at three wavelengths and at the same four lamp settings for the sphere. The radiance in the aperture was found to be uniform to within 0.6–2.2% (peak-to-valley variability), depending on the measurement conditions. This study was motivated by the requirement that the sphere source perform post-environmental calibrations of the SeaWiFS instrument, as well as to compare the various radiometric scales in use by the ocean color community which are all NIST traceable. The measurements in this report were made just before SIRREX-4.

1.1 INTRODUCTION

Broadband, uniform, large area sources can be used for absolute radiometric calibration of radiometric sensors if the relative spectral response of the sensor is known. Integrating sphere sources like the NASA GSFC sphere, which can be shipped to various sites, play a critical role in the calibration of field equipment, intercomparison of spectral radiance scales, and even in the calibration of satellite sensors themselves. The GSFC sphere was used at four SIRREXs, where intercomparisons were made with various sources and radiometers. It was used in October 1992 at Hughes Santa Barbara Remote Sensing (SBRS) in a comparison with the SBRS integrating sphere source that was used for the initial calibration of the SeaWiFS instrument shortly after it was built (Mueller 1993a).

The GSFC sphere is scheduled to be used for the post-environmental test calibration of SeaWiFS. The application motivated a careful study of the uniformity of the spectral radiance across the exit aperture using the SXR, a multichannel filter radiometer (Johnson et al. 1997), and a measurement of the spectral radiance of the sphere source from 370–1,100 nm. A prism-grating monochromator and a gas-filled tungsten strip lamp were used for these absolute measurements. The work was performed in the Optical Technology Division of NIST as part of an interagency agreement with NASA.

The GSFC sphere is 1.07 m (3.5 ft) in diameter; the exit aperture is 39.5 cm (15.5 in) in diameter. The sphere source was originally built for the National Oceanic and Atmospheric Administration (NOAA) and was acquired by GSFC in 1989; it is similar to that described in Hovis and Knoll (1983). As part of the NOAA programs, the sphere source was calibrated by Optronic Laboratories, Inc., and used to calibrate spectroradiometers that were flown on high altitude aircraft in a satellite underpass configuration over White Sands, New Mexico, in order to calibrate the fifth Land Resources Satellite (LANDSAT-5) Thematic Mapper (Smith et al. 1990), the Advanced Very High Resolution Radiometer (AVHRR) on NOAA-9 (Smith et al. 1988 and Smith et al. 1989a), and the Visible-Infrared Spin-Scan Radiometer (VISSR) on the sixth Geostationary Operational Environmental Satellite (GOES-6) spacecraft (Smith el al. 1989b).

The GSFC sphere is configured with 16 45 W quartz halogen lamps, which are mounted on the inside wall and surround the exit aperture. Small diffuse screens block the direct optical path between each lamp and the exit aper-

ture. The interior surface is coated with a paint containing barium sulfate. The source is cooled using a fan mounted on a baffled aperture on top of the sphere; air flows in the sphere through a filtered fan port at the top and then through a baffled aperture at the bottom. Four power supplies are used to operate the fan and the 16 lamps in a constant current mode of operation—one power supply for each set of four lamps; the four lamps are connected in series. Various radiance levels are achieved by turning off lamps associated with a particular power supply, followed by turning off the supplies (e.g., to transition from 13 lamps to 12 lamps, the fourth power supply is turned off). The sphere was recoated by GSFC in April 1994.

Prior characterizations and calibrations of the GSFC sphere were done at GSFC and at the SIRREX activities (Mueller 1993a, Mueller et al. 1994, Mueller et al. 1995, and Johnson et al. 1996). At GSFC, a NASA filter radiometer and the SXR were used to map the spectral radiance in the exit aperture (Mueller et al. 1994). GSFC also investigated the degree to which water vapor absorption affects the spectral radiance of the sphere using a single-grating monochromator, model 746 from Optronic Laboratories† with foreoptics (McLean, pers. comm.). The bulk of the measurements by GSFC, however, consists of determinations of the average spectral radiance of the exit aperture using a standard irradiance lamp and a double-aperture method for the irradiance-to-radiance transfer (e.g., Walker et al. 1987b, or Appendix A in Johnson et al. 1996). The collection optic for the monochromator is a small integrating sphere with a known aperture; this configuration is termed the 746/ISIC and it denotes the Optronic Laboratories model 746 monochromator equipped with an integrating sphere irradiance collector (ISIC).

At the annual SIRREX activities, the data were obtained on the sphere's temporal stability, radiance levels, and the degree to which Lambert's law is followed. At SIRREX-2, -3, and -4, information was obtained on the consistency of independent, NIST-traceable, spectral radiance scales by measuring the spectral radiance of the GSFC sphere using the 746/ISIC system and the SXR. The former is traceable to NIST via the irradiance scale assigned to an FEL 1,000 W tungsten-halogen standard lamp; the latter is traceable to NIST via the radiance scale assigned to a small integrating sphere source. Both of the NIST scales are derived using the same facility and starting point for the scale realization (Walker et al. 1987a and Walker et al. 1987b). The main results indicated that the radiance of the GSFC sphere was variable across the exit aperture, with peak-to-valley differences of about 3% (Mueller et al. 1994) and that the variability was reduced to about 0.5% after recoating the sphere walls. At SIRREX-2, the GSFC 746/ISIC and the SXR agreed to within 5% for measurements of the spectral radiance of the GSFC sphere. At SIRREX-3, the corresponding result was about 3% (Mueller et al. 1995).

The measurements reported here were done in April 1995 just prior to SIRREX-4 (Johnson et al. 1996). They were motivated by the opportunity to measure the response of the SeaWiFS instrument to the radiance from the GSFC sphere as part of post-environmental test calibrations at Orbital Sciences Corporation (OSC) (Barnes et al. 1994b). It was also a good opportunity to assign a spectral radiance scale directly to the GSFC sphere at NIST, so that the SXR and 746/ISIC measurements of the GSFC sphere at SIRREX-4 could be compared to a NIST radiance scale assigned to a gas-filled tungsten standard strip lamp. The GSFC sphere was operated at four radiance levels in this work by operating 16, 8, 4, and 1 lamp, which gave adequate overlap with the desired calibration levels for SeaWiFS (Barnes et al. 1994b).

1.2 APERTURE UNIFORMITY

To calibrate a radiometer, a source with known radiance (e.g., the exit aperture of a sphere) is aligned so that the entrance window of the radiometer is centered and coplanar with the source; the entrance pupil must be filled by the source as well. This part of the measurement equation (ignoring any spectral aspects) involves integrating the spectral radiance as a function of position and direction over the source area and all relevant directions, which depend on the location and size of the entrance pupil of the radiometer (Kostkowski and Nicodemus 1978). If the spectral radiance is uniform across the aperture and independent of viewing direction (lambertian), the measurement equation simplifies to a product of the spectral radiance and a geometric factor that can be measured (or calculated) and associated with the radiometer.

If the spectral radiance is nonuniform, the relative spatial response function of the radiometer must be measured. This relative spatial response corresponds to radiation from a point source at x,y when the radiometer is focused at 0,0. In turn, this quantity, the point-spread response (PSR), must be multiplied by the actual spatial distribution of the spectral radiance across the aperture. The product is then integrated, as described above, to estimate a correction factor for the source nonuniformity. In practice, it is more common to assign a value corresponding to a level of nonuniformity that will not affect the final results by more that some stated uncertainty, and then to measure the source in question to determine if it can be used in the calibration procedure. If the source does not meet the requirement, it is usually easier to improve the source than to calculate correction factors.

The measurement procedure consisted of mounting the SXR on an x,y translation stage 100 cm from the exit aperture of the GSFC sphere and recording the signal at one

† Identification of commercial equipment to adequately specify the experimental problem, does not imply recommendation or endorsement by NASA or NIST, nor does it imply that the equipment identified is necessarily the best available for the purpose.

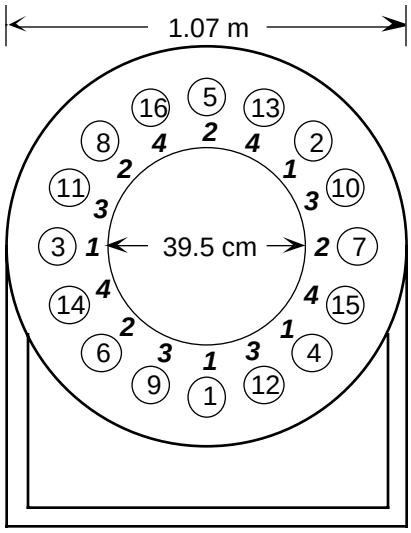

Fig. 1. The location of the 16 lamps in the GSFC sphere as observed when facing the sphere aperture. The lamp identification number is shown inside the small circles, and the power supply number (1–4) is given around the exit aperture (inner-most circle) in slanted type.

measurement wavelength, or SXR channel, for a grid of points covering the exit aperture. A 50×50 cm^2 area was measured with a step size of 5 cm, which was chosen because the target area viewed by the SXR at this distance is about 4.5 cm and the sphere aperture is 39.5 cm in diameter. A background signal was recorded by covering the objective lens of the SXR with the lens cap.

Four radiance levels of the sphere were measured, corresponding to having all 16 lamps on, then 8, 4, and 1. For each lamp configuration, the sphere was mapped at three SXR channels (wavelengths). The current, drawn by the lamp power supplies and the voltage across each lamp, was recorded prior to each spatial scan. The spatial scans and data acquisition were fully automated using a personal computer (PC), two Aerotech linear positioning stages with direct current (DC) servo motors, an Aerotech controller, and a Hewlett Packard (HP) 3457A digital voltmeter. The Institute of Electrical and Electronic Engineers (IEEE) 488 interface bus was used to establish communications, and the stage position and data acquisition software was written in Visual Basic.

Figure 1 shows the lamp arrangement for the GSFC sphere and the power supplies that control the lamps. Since the lamps require 20 minutes to stabilize, the most efficient measurement procedure was to start with all 16 lamps on, and then to turn off the selected lamps or power supplies for the other levels. The 16 lamp configuration results in symmetric illumination of the sphere, since the lamps are evenly spaced every 22.5°. As can be seen from Fig. 1, the eight-lamp configuration is also symmetric (power supplies 1 and 2), but the four- and one-lamp configurations are not symmetric (since lamps 1–4 and lamp 1 on power supply 1 were operated for these configurations).

It would be possible to operate the sphere in a symmetric manner with lamps 1, 2, 5, and 7, but this would require having two lamps off in both power supply 1 and 2. GSFC has never tried this configuration, and since they could not supply a wiring diagram of the system with details on how shunt resistors are used in place of a lamp when that lamp is turned off, only the normal procedure was used. It is not possible to operate the sphere with a single lamp and still produce a symmetric illumination field; the results indicate this configuration is the least uniform. Another disadvantage of the electrical system for the sphere is that the fan is operated on the power supply that operates lamps 1–4, so power supply 1 must always be on. Since GSFC does not advise the operation of a power supply without having at least one lamp on, lamps 1–4 get more use.

Table 1. Measurement configurations for the uniformity studies of the GSFC sphere.

Lamps	*SXR Wavelengths* [nm]		
1–16	411.5	441.6	661.8
1–8	411.5	487.1	661.8
1–4	411.5	487.1	661.8
1	411.5	548.0	661.8

Table 1 summarizes the measurement configurations for the uniformity studies. The choice of measurement wavelengths for the SXR was determined by:

1) Considering the amount of time available for the study,
2) The spectral coverage required,
3) The fact that the SXR has a more ideal PSR at particular channels, and
4) The relationship between the sphere radiance and the spectral bands of the SeaWiFS instrument that are appropriate for that radiance.

Table 2. Lamp parameters during uniformity measurements of the GSFC sphere.

Lamp	*Lamp Hours*		*Lamp Current* [A] *and Voltage* [V]							
Number	11 April	12 April	[A]	[V]	[A]	[V]	[A]	[V]	[A]	[V]
1	1.0	7.0	6.501	7.144	6.501	7.138	6.501	7.136	6.500	7.134
2		6.0	6.501	7.148	6.501	7.142	6.501	7.141		
3		6.0	6.501	6.984	6.501	6.977	6.501	6.976		
4		6.0	6.501	7.196	6.501	7.187	6.501	7.186		
5		4.5	6.500	7.065	6.499	7.057				
6		4.5	6.500	7.274	6.499	7.270				
7		4.5	6.500	7.144	6.499	7.140				
8		4.5	6.500	7.016	6.499	7.001				
9		2.5	6.501	7.173						
10		2.5	6.501	7.359						
11		2.5	6.501	7.200						
12		2.5	6.501	7.138						
13		2.5	6.500	7.237						
14		2.5	6.500	7.192						
15		2.5	6.500	7.159						
16		2.5	6.500	7.455						

The SXR was operated at an overall gain of unity and the digital voltmeter was programmed to average over 10 power line cycles, with the autozero mode enabled, and the number of samples set to 10. At each position, five readings of the digital voltmeter were recorded, and the five results along with the average and standard deviation were stored in an American Standard Code for Information Interchange (ASCII) file.

The standard deviations for the measurements in the exit aperture corresponded to a relative standard uncertainty of approximately 0.003%. The procedures for each measurement consisted of recording the lamp settings in a laboratory notebook, measuring the SXR background signal, and entering this value in the data acquisition program. Then, under computer control, the signal at the center coordinates for the scan was measured, and a horizontal scan from left to right (facing the sphere) at the lowest vertical position was made. The horizontal scans were repeated for all the vertical positions, and two readings at the center coordinates were made between each horizontal scan. The data files consist of a header section containing the relevant information followed by the stage position and signal data. Each complete mapping took about 25 minutes.

The average current and voltages for the lamps during the three measurements for each radiance level of the GSFC sphere are given in Table 2, as well as the number of hours that the lamps were operated for these tests (11 and 12 April 1995). For all of the measurements, the current for each set of four lamps was stable to within 1 mA, which corresponded to the precision of the indicators on the power supplies. The voltage for a particular lamp was stable to within 1 mV during a given lamp configuration, and changed by as much as 15 mV when going from the 16-lamp to the 8-lamp configuration. The repeat measurements at the center of the scan indicate that the combination of the GSFC sphere radiance and the SXR was stable to between 0.005–0.05%, except in the case of the measurement at 411.5 nm in the single lamp configuration, when this value was 0.14%. These variations correspond to the standard deviation of the measurements at the center of the scan position.

The results are shown in Figs. 2–5 in the form of contour plots. The net average signal at each scan position was normalized by the average of the net signal recorded for the center scan position. Scan positions that corresponded to a view of the edge of the sphere aperture were excluded. The 16-lamp configuration is shown in Fig. 2, the 8-lamp in Fig. 3, the 4-lamp in Fig. 4, and the 1-lamp in Fig. 5. The minimum contour corresponds to a square about 30 cm on a side. Within the square, the maximum and the minimum value for the normalized net signals are also indicated for each of the three wavelengths and the four radiance levels. All of the data indicate a local minimum in the upper left-hand quadrant when facing the sphere, and there seems to be little dependence on wavelength for a given lamp configuration.

Table 3 summarizes all of the results in terms of the peak-to-valley variability using the minimum and maximum values. The 16-lamp and 8-lamp configurations show similar variability, between 0.6–0.9%. The variability of the 4-lamp configuration is greater, between 1.1–1.2%, and the pattern of variability is consistent with the lamp arrangement (Fig. 1). The greatest variability is observed for the 1-lamp configuration, between 2.1–2.3%, and again the pattern is consistent with the lamp arrangement.

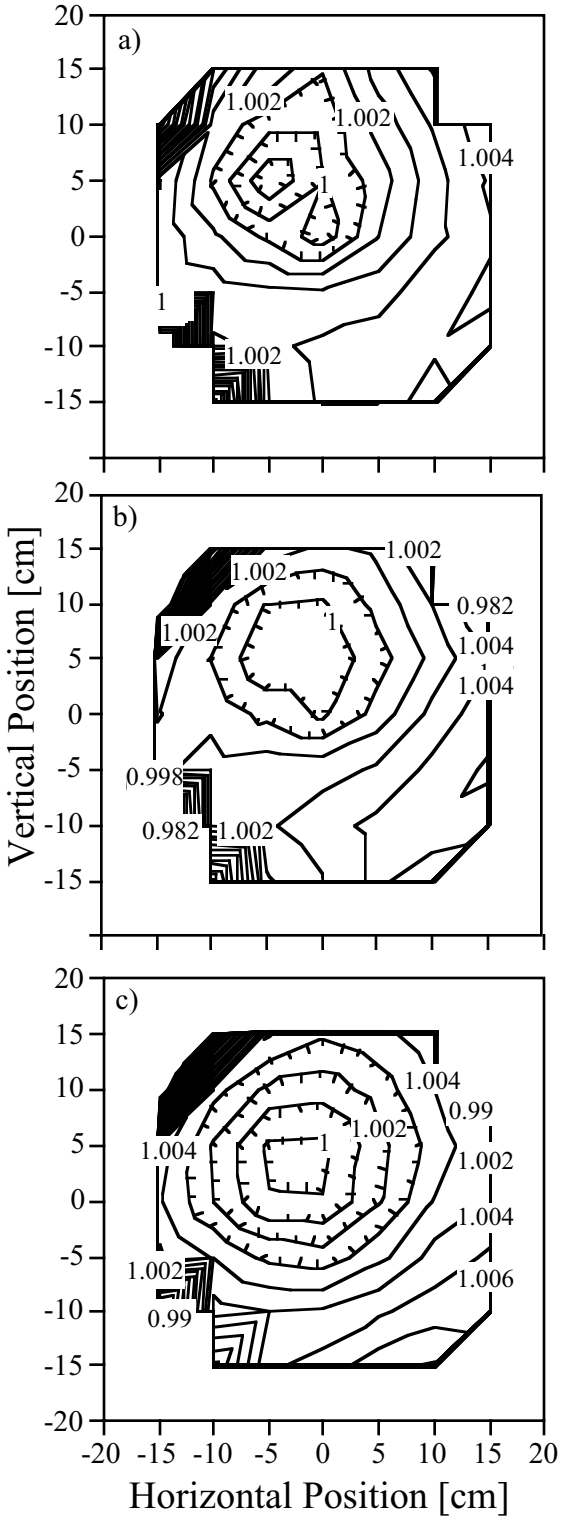

Fig. 2. Contour plot of the radiance in the exit aperture normalized to the average of the measurements at the center position of the GSFC sphere as measured with the SXR at **a)** 411.5 nm, **b)** 441.6 nm, and **c)** 661.8 nm with lamps 1–16 at 6.5 A. The values in the plots indicate the ratio of the radiance along the contour to the radiance at the center. The short lines perpendicular to the contours indicate that the radiance is decreasing in that direction.

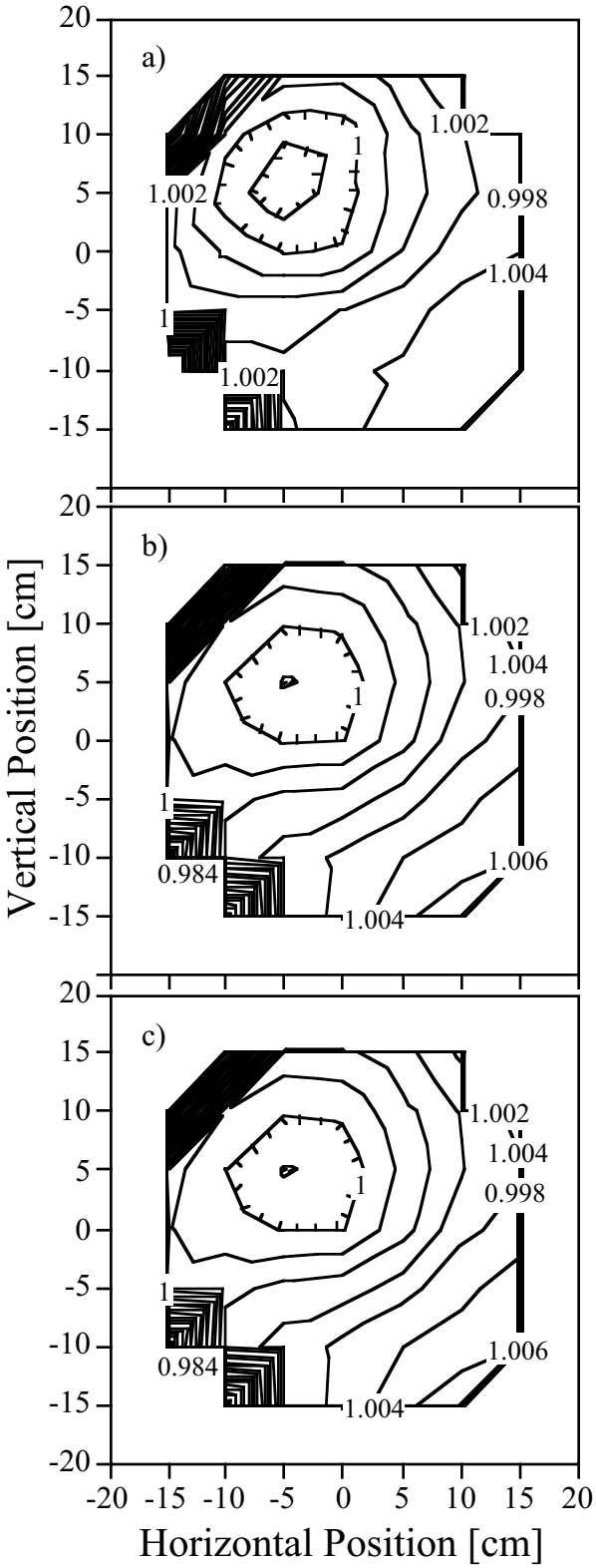

Fig. 3. Contour plot of the radiance in the exit aperture normalized to the average of the measurements at the center position of the GSFC sphere as measured with the SXR at **a)** 411.5 nm, **b)** 487.1 nm, and **c)** 661.8 nm with lamps 1–8 at 6.5 A. The values in the plots indicate the ratio of the radiance along the contour to the radiance at the center. The short lines perpendicular to the contours indicate that the radiance is decreasing in that direction.

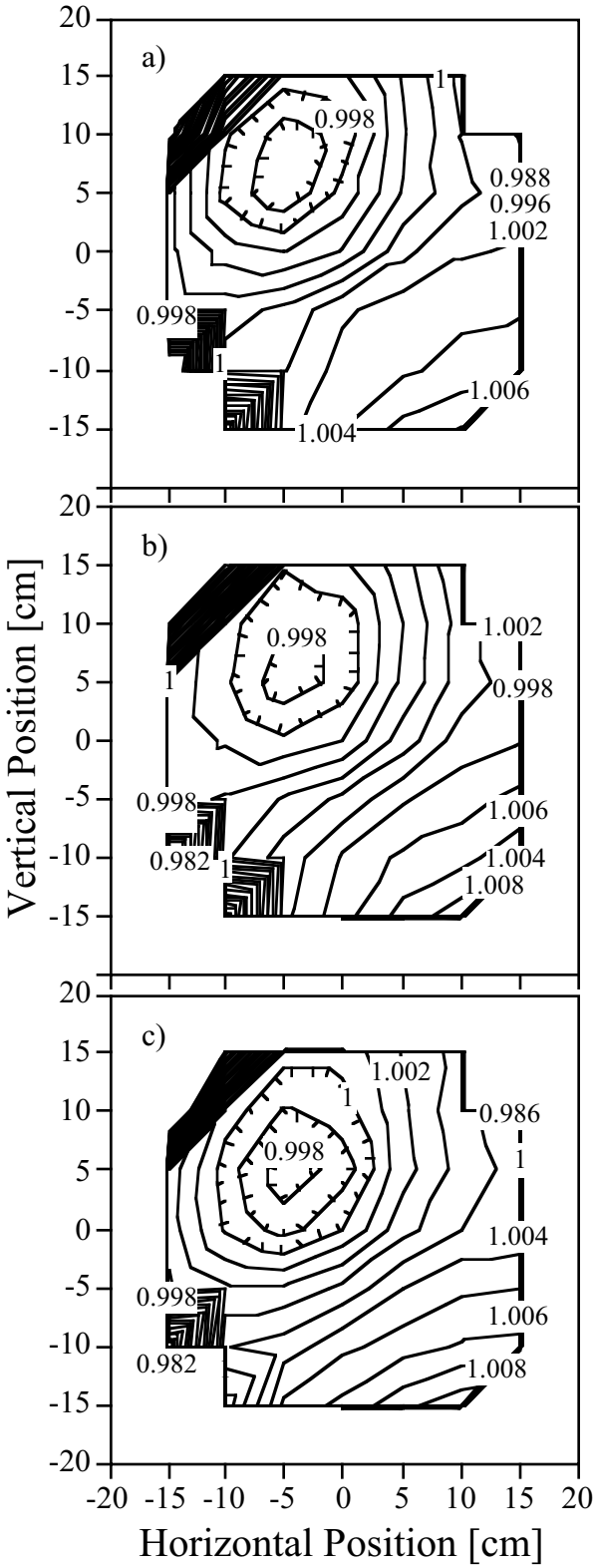

Fig. 4. Contour plot of the radiance in the exit aperture normalized to the average of the measurements at the center position of the GSFC sphere as measured with the SXR at **a)** 411.5 nm, **b)** 487.1 nm, and **c)** 661.8 nm with lamps 1–4 at 6.5 A. The values in the plots indicate the ratio of the radiance along the contour to the radiance at the center. The short lines perpendicular to the contours indicate that the radiance is decreasing in that direction.

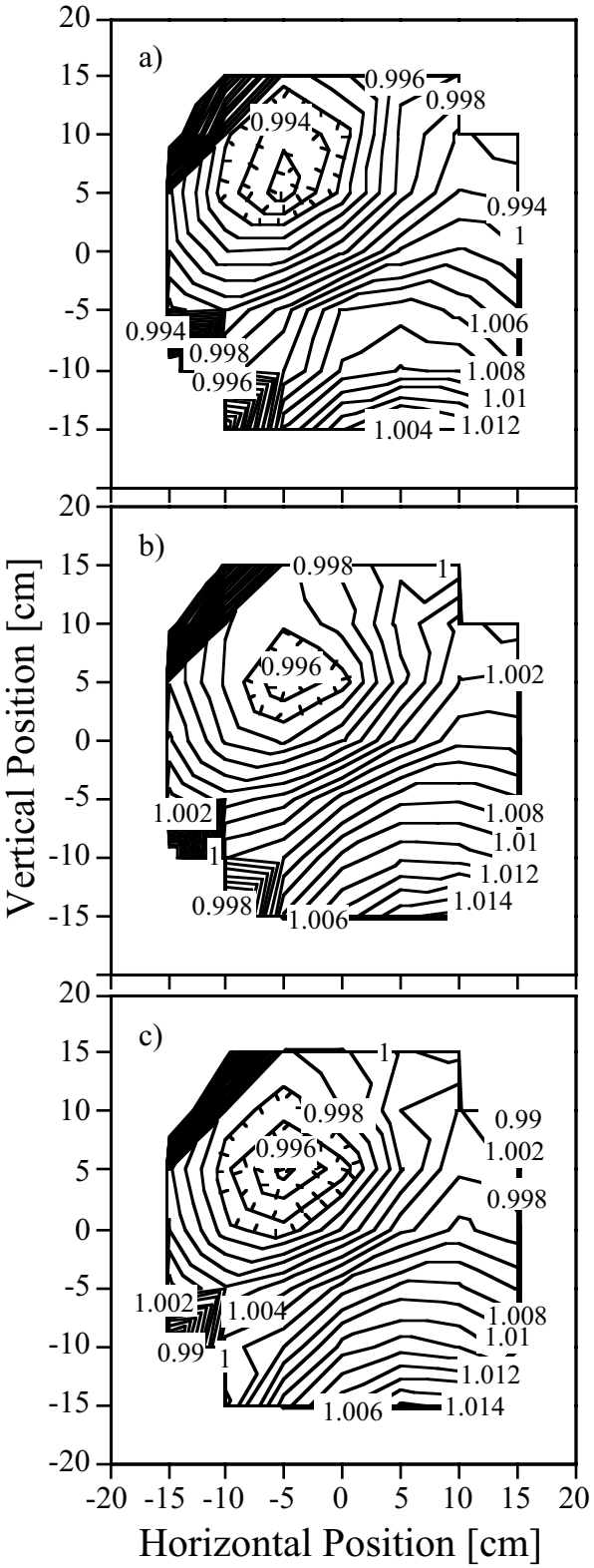

Fig. 5. Contour plot of the radiance in the exit aperture normalized to the average of the measurements at the center position of the GSFC sphere as measured with the SXR at **a)** 411.5 nm, **b)** 548.0 nm, and **c)** 661.8 nm with lamp 1 at 6.5 A. The values in the plots indicate the ratio of the radiance along the contour to the radiance at the center. The short lines perpendicular to the contours indicate that the radiance is decreasing in that direction.

Table 3. Results of the uniformity studies for the GSFC sphere presented as the peak-to-valley variability in percent.

Lamps	*SXR Wavelengths* [nm]				
On	411.5	441.6	487.1	548.0	661.8
1–16	0.76	0.61			0.84
1–8	0.67		0.78		0.87
1–4	1.10		1.14		1.24
1	2.27			2.14	2.15

1.3 SPECTRAL RADIANCE

The spectral radiance at the center of the exit port of the GSFC integrating sphere source was determined at wavelengths from 380–1,100 nm with 16, 8, 4, and 1 lamp operating. Signals as a function of wavelength from both a calibrated radiance source and from the sphere were measured, and the spectral radiance of the sphere was determined by the following procedure. Assuming $\hat{S}$ and $\tilde{S}$ are the signals from sources with known and unknown spectral radiance, respectively, the simplest measurement equation for these signals is given by

$$\hat{S} = \hat{L}R \tag{1}$$

and

$$\tilde{S} = \tilde{L}R \tag{2}$$

where $\hat{L}$ and $\tilde{L}$ are the known and unknown spectral radiances of the sources, respectively, and R is the spectral radiance responsivity (SRR) of the detector system. Measuring the signal from a source with a known spectral radiance, therefore, determines the SRR of the detector, from (1), which is then used in (2) along with the measured signal from the source with the unknown radiance to determine the spectral radiance of the unknown source.

The effects of radiant flux from wavelengths outside of the nominal spectral bandpass of the detector have been neglected in (1) and (2), as well as effects from a nonlinear response of the detector. To minimize these effects as much as possible, the known and unknown spectral radiances of the sources should be as similar as possible. For the measurements described in this effort, this was achieved by determining the spectral radiance of the sphere with 16 lamps operating from the known spectral radiance of a gas filament lamp. The spectral radiance of the sphere with 16 lamps operating was then used to determine the spectral radiance of the sphere with 8, 4, and 1 lamp operating.

1.3.1 Experimental Procedures

1.3.1.1 Equipment

The GSFC integrating sphere source and its accompanying power supply were described in Sect. 1.1. The source of known spectral radiance was a gas-filled tungsten ribbon filament lamp with the designation 92–04. This lamp was calibrated for spectral radiance by the Facility for Automated Spectroradiometric Calibrations (FASCAL) at NIST. The current through the lamp was supplied by an HP 6032A power supply and monitored by an HP 3457A digital voltmeter which measured the voltage across a calibrated shunt resistor. The detector system consisted of imaging optics, a prism-grating double monochromator with adjustable slit widths, and a silicon photodiode with an adjustable gain. A metal mask with a $0.6 \times 0.8\,\mathrm{mm}^2$ hole in front of the entrance slit of the monochromator defined the imaged area of the source. Details of this system can be found in Mielenz et al. (1990).

The voltage output of the silicon photodiode was measured by an HP 3457A digital voltmeter. The entire detector system was mounted in a box on a carriage which was translated horizontally to view either the filament lamp or the integrating sphere. The wavelength of the monochromator and the position of the carriage were under computer control; the computer recorded the monochromator wavelength as determined by an absolute encoder, and the voltage from the silicon photodiode was measured by the voltmeter. A measurement generally consisted of a wavelength scan over a given range, in which the signal from the photodiode was recorded at discrete wavelengths within the range.

1.3.1.2 Auxiliary Calibrations

Two calibrations were performed prior to measuring the spectral radiance of the integrating sphere. The first determined the actual wavelength setting of the monochromator in terms of the wavelength measured by the encoder, while the second determined the ratio of the gains of the silicon photodiode.

The wavelength calibration of the monochromator was determined by viewing, with the detector system, the exit port of a small integrating sphere which had a line source at the entrance port. The line source was either a HeNe laser or a gas emission lamp. Wavelength scans were performed over ranges that included the line source wavelengths. The HeNe laser line at 632.816 nm was scanned with monochromator slit widths ranging from 0.125–1.000 mm. From these scans, the bandwidth of the monochromator was determined from the difference in wavelengths at which the signals were half that of the maximum signal. The dispersion of the monochromator is approximately $4.25\,\mathrm{nm\,mm}^{-1}$ at 632.8 nm and increases slightly with a decrease in slit width. The centroids of the HeNe laser line were also determined from these scans, and were all within 0.015 nm of each other; thus, the slit width has a minimal effect on the centroid of a line source.

Gas emission lamps were chosen which had intense singlet lines, within the wavelength range 350–1,100 nm, and were separated from other lines by at least 2 nm. Wavelength scans of the lines from Ar, Hg, Ne, and Xe lamps

were usually performed with 0.25 mm slit widths at 0.05 nm intervals over 4 nm ranges centered on the wavelengths of the lines. A few of the scans of lines from the Ne lamp were performed with 0.125 mm slit widths in order to resolve the lines that are close together in wavelength. The centroids of the emission lines, in terms of the encoder wavelength, were calculated from the scans, and the differences between the actual wavelengths of the lines and the centroid wavelengths as a function of centroid wavelength were fit with a third-order polynomial. The actual wavelength of the monochromator, therefore, is given by the encoder wavelength plus the fit of the difference. Using this calibration, the standard uncertainty in the wavelength of the monochromator was 0.2 nm.

While the magnitude of the spectral radiance of the gas filament lamp was several times that of the sphere with 16 lamps operating, the spectral distribution was similar. Therefore, effects from stray light in the detector system were minimized, but different gains for the photodiode had to be used when measuring the two sources. The gain ratio is simply the ratio of the higher gain to the lower gain, and is equal to the ratio of the signals at those two gains. The gain ratio was determined by viewing the gas filament lamp, fixing the wavelength of the monochromator at 700 nm, and recording the signals from the silicon photodiode at consecutive gain settings. The slit width was adjusted so that a nearly full-scale signal was obtained at the higher gain setting. Average signals were determined four times at gains of 10^8, 10^9, and 10^{10} with slit widths of 0.3 mm and 1.2 mm. The gain ratio for gains of 10^{10} and 10^8 was 99.975751 $\pm$ 0.011240.

1.3.1.3 Alignment

Proper alignment of both the gas filament lamp and the exit port of the integrating sphere with the optic axis of the detector system is critical for correctly determining the spectral radiance of the integrating sphere. The beam from a HeNe laser mounted behind the exit slit of the monochromator, and passing through the monochromator and the imaging optics, defined the optic axis for the detector system.

The gas filament lamp was mounted on a bipost base attached to tilt and translation stages on an optical table. The lamp was operated at half its normal current for the purpose of optical alignment. Tilt and translation stages were adjusted so that the laser beam defining the optic axis passed through the notch in the lamp filament, as well as the tip of an arrow etched into the back of the lamp envelope. This oriented the filament perpendicular to, and centered vertically on, the optic axis. The lamp was then translated to center the laser beam horizontally on the filament. Finally, the lamp was translated along the optic axis to focus the image of the filament onto the mask, which is in front of the entrance slit of the monochromator.

The integrating sphere was placed on the floor next to the optical table. The front of the exit aperture of the sphere was placed the same distance—29.0 cm—from the detector system, as was the gas filament lamp. The center of the cover of the exit aperture was marked previously with a cross, and a glass slide was placed over it. Both the rotation of the integrating sphere about a vertical axis and the height of the rear sphere frame were adjusted to reflect the laser beam back onto itself, thereby making the exit aperture perpendicular to the optic axis. The height of the integrating sphere and the position of the carriage were adjusted to center the exit aperture on the optic axis. These rotation and height adjustments were iterated several times to center the laser beam on the cross and reflect it back off itself. The exit aperture was centered to within 2 mm, but the cover over the exit aperture was slightly bowed, so the optic axis was perpendicular to the exit aperture to within 2°.

The SXR was placed on a tripod behind the carriage containing the detector system and oriented to view the center of the exit aperture of the integrating sphere. The distance from the exit aperture to the front plate of the SXR was 136 cm.

1.3.1.4 With 16 Lamps

The gas filament lamp was operated at 41.6 A, the same current at which it was calibrated for spectral radiance at FASCAL, with an uncertainty of 0.2 mA. All 16 of the lamps of the integrating sphere were operated at 6.5 A. The slit width of the monochromator was chosen by setting the wavelength to 670 nm, viewing the gas lamp, and adjusting the slit width to yield a signal close to the full scale for that gain setting. This resulted in a slit width of 0.9 mm, corresponding to a bandpass of 4.2 nm at a wavelength of 632.8 nm. The voltmeter was configured to average over 100 power line cycles and to autozero.

Wavelength scans of both the gas filament lamp and the integrating sphere were performed from 360–1,100 nm at 10 nm increments, and took 20 minutes to complete. Three voltage signals were recorded at each wavelength, and gains of 10^8 and 10^{10} on the silicon photodiode were used with the gas filament lamp and the integrating sphere, respectively. The gas filament lamp was scanned first, and then the carriage with the detector system was translated to view the integrating sphere. Another wavelength scan was performed, and the process was completed by translating the carriage back to the gas filament lamp for a final wavelength scan. The radiance of the integrating sphere was measured with the SXR before and after each wavelength scan with the detector system.

1.3.1.5 With 8, 4, and 1 Lamp

The procedure for measuring the radiance of the integrating sphere with 8, 4, and 1 lamp was similar to that given above for 16 lamps. The slit width was increased to 3.0 mm (12 nm bandpass) in order to maximize the signals

from the integrating sphere when all 16 lamps were operating, and the gain of the silicon photodiode was fixed at 10^{10}. Wavelength scans of the integrating sphere were performed with 16, 8, 4, and 1 lamp operating, and the radiance was measured by the SXR before and after each scan. After all the lamps were turned off, the background signal of the silicon photodiode was determined at each gain. This background signal was $-6.733 \times 10^{-5}\,\mathrm{V} \pm 0.846 \times 10^{-5}\,\mathrm{V}$ at a gain of 10^8 and $6.0771 \times 10^{-4}\,\mathrm{V} \pm 3.1762 \times 10^{-4}\,\mathrm{V}$ at a gain of 10^{10}.

The total accumulated operating time for the lamps of the integrating sphere during these measurements was 9 hours for lamp 1, 8.5 hours for lamps 2–4, 8 hours for lamps 5–8, and 7.5 hours for lamps 9–16. The voltages across the lamps were comparable to those listed in Table 2, with variations in the voltage of each lamp on the order of several tens of millivolts.

1.3.2 Results

For each wavelength scan, the data were reduced to an average corrected signal as a function of wavelength. First, the wavelength of the monochromator, given by the encoder, was converted to the actual wavelength using the results from the calibration process (Sect. 1.3.1.2). Second, the three voltage measurements at each wavelength were averaged with the standard uncertainty given by the standard deviation of the mean. Third, the background signal of the photodiode for that gain was subtracted from the average signal, and the standard uncertainty of the background signal was propagated. The resulting signal as a function of wavelength was fit with a natural cubic spline to wavelengths from 380–1,100 nm at 10 nm increments. The standard uncertainty of the fit signal was taken to be the standard uncertainty of the signal at the actual wavelength closest to the fit wavelength.

1.3.2.1 With 16 Lamps

The spectral radiance of the gas filament lamp had been determined by FASCAL at 34 wavelengths from 225–2,400 nm, and the standard uncertainty was given at seven of those wavelengths. Both the spectral radiance and the standard uncertainty as a function of wavelength were fit with a natural cubic spline to the wavelength range 380–1,100 nm at 10 nm increments. The corrected, average signals from both scans of the gas filament lamp were averaged and the uncertainties of the signals were propagated. These final signals were divided by the spectral radiance to obtain the SRR of the detector system with slit widths of 0.9 mm and a gain of 10^8. The results are shown in Fig. 6a, where the SRR is plotted as a function of wavelength. The SRR has abrupt changes near 580, 780, and 980 nm, which are caused by the optics of the detector system.

The spectral radiance of the integrating sphere with all 16 lamps operating was obtained by dividing the averaged, corrected, and fitted signal by the SRR, determined in the preceding paragraph, and by the gain ratio determined in Sect. 1.3.1.2. The spectral radiance at 760 nm was obviously low when compared to the spectral radiances at neighboring wavelengths. This was due to the local minimum in the SRR at that wavelength, as shown in Fig. 6a. Consequently, the spectral radiance from 660–860 nm, excluding the value at 760 nm, was fit with a second-order polynomial, and this fit was used to calculate the spectral radiance at 760 nm. The resulting radiance, as a function of wavelength, is plotted in Fig. 6b.

Sources of uncertainty in the spectral radiance of the integrating sphere arise from the gas filament lamp radiance and current, the detector system signals and wavelength, and the sphere alignment. The standard uncertainty in the spectral radiance of the gas filament lamp is given from the calibration performed by FASCAL. The 2 mA uncertainty in the current through the lamp yields a relative standard uncertainty in the spectral radiance dL/L given by

$$\frac{dL}{L} = \left[\frac{654.6}{\lambda}\right] 0.00013\, dI, \tag{3}$$

where λ is the wavelength in nanometers and dI is the current standard uncertainty in milliamps (Walker et al. 1987b).

The standard uncertainty in the signal is the propagation of the uncertainties from the average signals, the background signal, and the gain ratio. The relative standard uncertainty in radiance due to an uncertainty in the wavelength is given by the following:

$$\frac{dL}{L} = \frac{dL}{d\lambda}\frac{d\lambda}{L}. \tag{4}$$

An analytical expression for the derivative of the radiance with respect to wavelength was obtained by differentiating the Wien radiation law. Fits of the spectral radiance of each source to the Wien radiation law were used to obtain the parameters needed for the analytic expression.

The results of the SIRREX-3 activity (Mueller et al. 1995) show that the maximum change in radiance as a function of viewing angle is 1.2% at 5°; therefore, assuming a maximum uncertainty of 2° along either the horizontal or the vertical axis, the relative standard uncertainty is approximately 0.0020. The relative standard uncertainties, from each of the sources detailed here in determining the spectral radiance of the integrating sphere with 16 lamps operating, are given in Table 4 (at four selected wavelengths). Both the detector signal and the wavelength become significant sources of uncertainty at the shorter wavelengths.

1.3.2.2 With 8, 4, and 1 Lamp

The SRR of the detector system with the larger slit widths and higher gain used with 8, 4, and 1 lamp operating was obtained from the wavelength scan of the integrating sphere with 16 lamps operating. The average, corrected, fit signals from this scan were divided by the spectral radiance, calculated in the preceding section, to yield

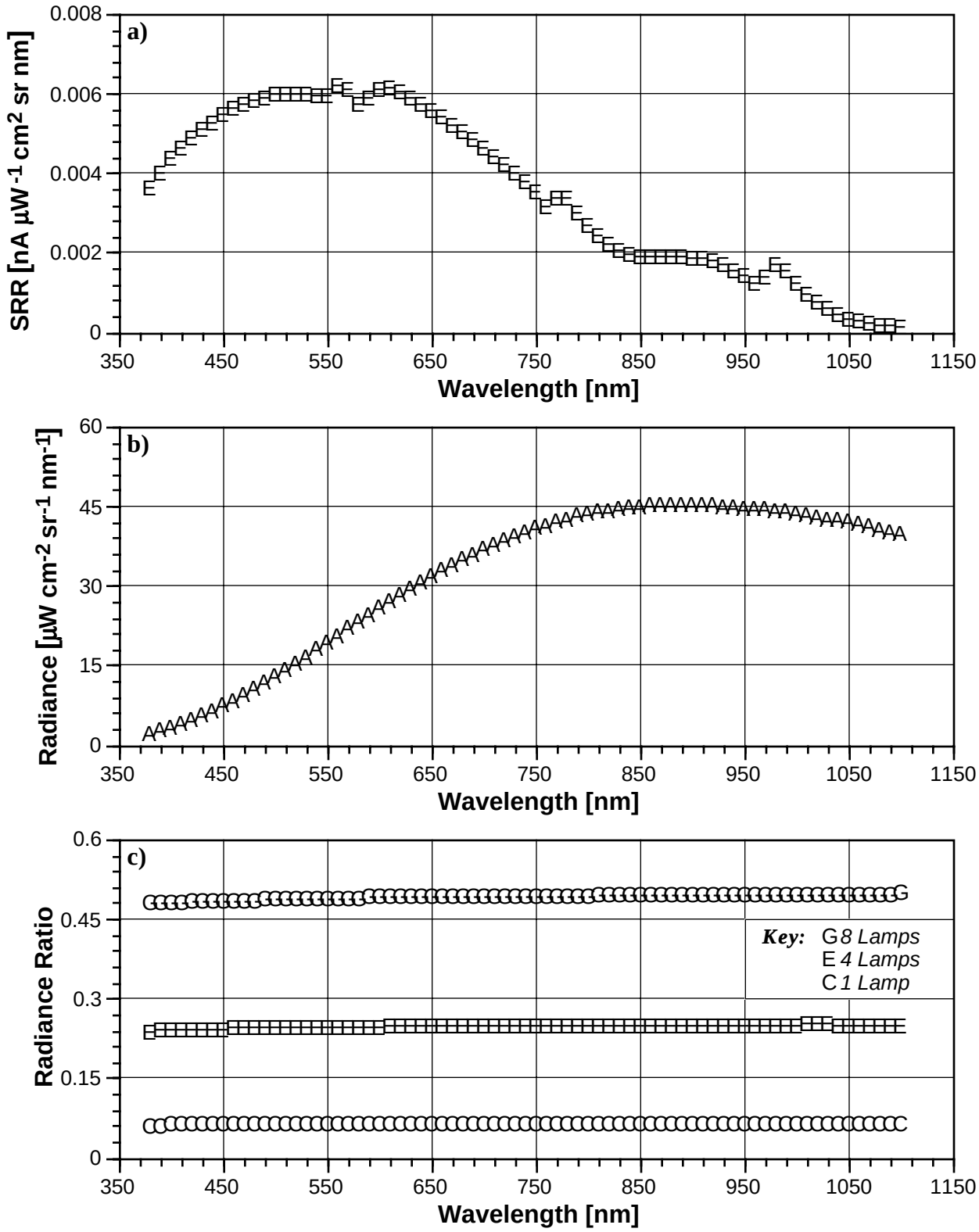

Fig. 6. Radiance analyses for the calibration of the GSFC sphere: **a)** SRR as a function of wavelength as determined from the gas filament lamp at a gain of 10^8 and a slit width of 0.9 mm; **b)** radiance as a function of wavelength at the center of the exit aperture of the GSFC sphere with 16 lamps operating; and **c)** the ratio of radiance of the integrating sphere with the indicated number of lamps operating to the radiance with 16 lamps operating as a function of wavelength.

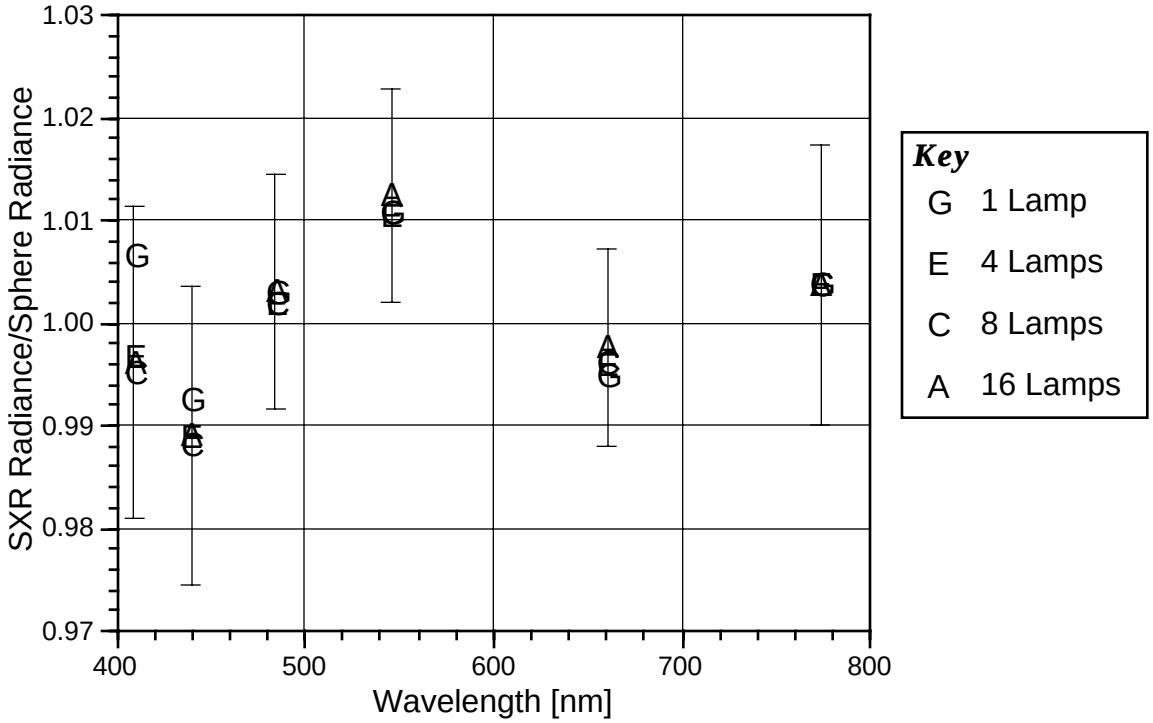

Fig. 7. Spectral radiance comparison of the GSFC sphere calibration with the standard lamp and spectroradiometer compared to the SXR measurements that were made during the calibration procedure. The different symbols correspond to the lamp configuration; the relative uncertainties in the SXR measurements are indicated by the vertical bars for the 16 lamp configuration.

the SRR. This responsivity has the same spectral shape as that shown in Fig. 6a, although it is larger in magnitude because of the larger slit widths and higher gain. Also, this SRR was determined only once since no lamps were operating after the series of measurements, detailed in this section, were complete.

Table 4. The relative standard uncertainties (in percent) from the indicated sources at the given wavelengths for the spectral radiance of the GSFC sphere with 16 lamps operating.

Source of Uncertainty	*Wavelength* [nm]			
	400	600	800	1,000
Lamp Radiance	0.44	0.33	0.29	0.27
Lamp Current	0.02	0.02	0.01	0.01
Detector Signal	0.14	0.03	0.03	0.03
Detector Wavelength	0.26	0.08	0.02	0.00
Sphere Alignment	0.10	0.10	0.10	0.10
RSS† Total	0.54	0.35	0.31	0.29

† Root sum squared.

The spectral radiance of the integrating sphere with 8, 4, and 1 lamp operating was obtained by dividing the average, corrected, fit signal from the wavelength scan with each lamp combination by the SRR. Again, while the shape of the spectral radiance for each lamp combination is similar to that shown in Fig. 6b, the magnitude decreases with decreasing number of operating lamps, as expected. The ratio of the spectral radiance with a given number of lamps operating to the spectral radiance with 16 lamps operating, is given in Fig. 6c as a function of wavelength. The ratios are all less than the nominal values of 0.5, 0.25, and 0.0625 for 8, 4, and 1 lamp, respectively, but approach these values at longer wavelengths. The spectral radiance of the integrating sphere at each lamp combination, along with the relative standard uncertainty, is given in Table 5.

The number of sources of uncertainty in the spectral radiance are considerably reduced from those of the preceding section. The uncertainties in the spectral radiance with 16 lamps operating are given by the results from the preceding section, and those from the detector signals are still present. However, the uncertainty in radiance from the current through the lamps of the integrating sphere is unknown, and the encoder wavelengths and sphere alignment are unchanged for all the wavelength scans, so there is no uncertainty associated with them.

1.4 Ancillary SXR Measurements

In order to track the performance of the GSFC sphere during SIRREX-4, as well as the post-environmental SeaWiFS calibration, the SXR was used to measure the spectral radiance of the GSFC sphere for the four radiance levels in between the measurements with the spectroradiometer. These measurements were compared by fitting

Table 5. The radiance, L [μW cm^{-2} nm^{-1} sr^{-1}], and relative standard uncertainty, δ [%], as a function of wavelength, λ, of the GSFC sphere with the indicated number of lamps operating.

λ	*16 Lamps*		*8 Lamps*		*4 Lamps*		*1 Lamp*		λ	*16 Lamps*		*8 Lamps*		*4 Lamps*		*1 Lamp*	
[nm]	L	δ	L	δ	L	δ	L	δ	[nm]	L	δ	L	δ	L	δ	L	δ
380	1.943	0.61	0.926	0.68	0.457	0.74	0.113	1.51	750	40.64	0.31	19.95	0.32	9.987	0.32	2.534	0.32
390	2.449	0.57	1.170	0.61	0.579	0.64	0.145	1.13	760	41.27	0.31	20.27	0.31	10.15	0.31	2.573	0.32
400	3.047	0.54	1.459	0.56	0.723	0.58	0.182	0.90	770	41.90	0.31	20.59	0.31	10.31	0.31	2.614	0.32
410	3.753	0.51	1.801	0.53	0.894	0.54	0.226	0.75	780	42.45	0.31	20.86	0.31	10.45	0.31	2.647	0.32
420	4.536	0.50	2.179	0.51	1.082	0.52	0.275	0.66	790	42.94	0.31	21.11	0.31	10.57	0.31	2.677	0.32
430	5.357	0.49	2.576	0.50	1.280	0.50	0.326	0.60	800	43.37	0.31	21.33	0.31	10.68	0.31	2.704	0.32
440	6.239	0.47	3.005	0.49	1.494	0.49	0.380	0.56	810	43.75	0.31	21.53	0.31	10.79	0.31	2.729	0.32
450	7.181	0.46	3.462	0.46	1.722	0.46	0.439	0.52	820	44.05	0.31	21.67	0.31	10.85	0.31	2.745	0.32
460	8.188	0.45	3.952	0.45	1.967	0.45	0.502	0.49	830	44.35	0.30	21.83	0.30	10.93	0.31	2.764	0.32
470	9.251	0.44	4.470	0.44	2.226	0.44	0.568	0.47	840	44.63	0.30	21.97	0.31	11.01	0.31	2.782	0.32
480	10.36	0.43	5.014	0.44	2.497	0.44	0.637	0.47	850	44.82	0.30	22.07	0.30	11.06	0.30	2.794	0.32
490	11.52	0.42	5.580	0.42	2.781	0.42	0.709	0.44	860	44.99	0.30	22.16	0.30	11.10	0.30	2.805	0.32
500	12.73	0.41	6.170	0.42	3.075	0.42	0.784	0.43	870	45.10	0.30	22.22	0.30	11.14	0.30	2.813	0.32
510	13.96	0.40	6.772	0.41	3.377	0.41	0.861	0.42	880	45.17	0.30	22.26	0.30	11.16	0.30	2.818	0.32
520	15.22	0.40	7.392	0.40	3.686	0.40	0.940	0.41	890	45.21	0.30	22.28	0.30	11.17	0.30	2.821	0.32
530	16.51	0.39	8.023	0.39	4.002	0.39	1.021	0.40	900	45.10	0.30	22.24	0.30	11.15	0.30	2.815	0.32
540	17.80	0.38	8.659	0.39	4.321	0.39	1.102	0.40	910	45.04	0.30	22.21	0.30	11.14	0.30	2.811	0.32
550	19.12	0.38	9.306	0.38	4.645	0.38	1.184	0.39	920	45.01	0.30	22.20	0.30	11.13	0.30	2.809	0.32
560	20.43	0.37	9.955	0.37	4.970	0.37	1.267	0.38	930	44.72	0.29	22.06	0.30	11.06	0.30	2.792	0.32
570	21.76	0.37	10.61	0.37	5.297	0.37	1.350	0.38	940	44.56	0.29	21.98	0.29	11.03	0.30	2.781	0.32
580	23.05	0.36	11.24	0.37	5.615	0.37	1.431	0.37	950	44.26	0.29	21.84	0.29	10.96	0.30	2.763	0.33
590	24.34	0.36	11.88	0.36	5.936	0.36	1.514	0.36	960	44.23	0.29	21.83	0.30	10.95	0.30	2.760	0.34
600	25.61	0.35	12.51	0.35	6.250	0.35	1.593	0.36	970	44.14	0.29	21.80	0.29	10.94	0.29	2.757	0.33
610	26.86	0.35	13.13	0.35	6.559	0.35	1.672	0.36	980	43.90	0.29	21.69	0.29	10.88	0.29	2.744	0.32
620	28.10	0.34	13.74	0.34	6.865	0.34	1.750	0.35	990	43.71	0.29	21.59	0.29	10.83	0.29	2.729	0.32
630	29.29	0.34	14.33	0.34	7.161	0.34	1.824	0.35	1,000	43.41	0.29	21.45	0.29	10.76	0.29	2.708	0.34
640	30.45	0.33	14.90	0.34	7.451	0.34	1.898	0.34	1,010	43.12	0.29	21.33	0.29	10.70	0.30	2.690	0.37
650	31.62	0.33	15.48	0.33	7.742	0.33	1.971	0.34	1,020	42.82	0.29	21.19	0.30	10.62	0.31	2.669	0.42
660	32.70	0.33	16.02	0.33	8.011	0.33	2.039	0.34	1,030	42.48	0.29	21.03	0.31	10.54	0.32	2.643	0.49
670	33.76	0.33	16.55	0.33	8.278	0.33	2.106	0.33	1,040	42.14	0.30	20.86	0.32	10.45	0.34	2.618	0.60
680	34.77	0.32	17.05	0.32	8.528	0.32	2.169	0.33	1,050	41.78	0.31	20.70	0.34	10.36	0.37	2.591	0.75
690	35.71	0.32	17.52	0.32	8.766	0.32	2.229	0.33	1,060	41.36	0.33	20.48	0.39	10.24	0.43	2.559	0.97
700	36.67	0.32	18.00	0.32	9.006	0.32	2.289	0.33	1,070	40.93	0.35	20.25	0.45	10.12	0.51	2.530	1.24
710	37.55	0.32	18.44	0.32	9.227	0.32	2.344	0.32	1,080	40.48	0.40	20.04	0.53	10.00	0.62	2.504	1.58
720	38.35	0.32	18.84	0.32	9.430	0.32	2.395	0.32	1,090	40.04	0.46	19.83	0.64	9.883	0.77	2.486	2.01
730	39.16	0.31	19.24	0.32	9.632	0.32	2.446	0.32	1,100	39.62	0.55	19.65	0.81	9.759	0.97	2.483	2.58
740	39.93	0.31	19.62	0.31	9.824	0.31	2.493	0.32									

Table 6. A comparison of SXR spectral radiance measurements (L_S) to the values measured with the spectroradiometer and the gas-filled strip lamp standard (L_G), both given in units of μW cm^{-2} nm^{-1} sr^{-1}.

λ	*16 Lamps*			*8 Lamps*			*4 Lamps*			*1 Lamp*		
[nm]	L_S	L_G	L_S/L_G	L_S	L_G	L_S/L_G	L_S	L_G	L_S/L_G	L_S	L_G	L_S/L_G
411.5	3.853	3.869	0.9959	1.848	1.857	0.9951	0.9188	0.9220	0.9965	0.2349	0.2335	1.006
441.6	6.317	6.387	0.9890	3.040	3.077	0.9881	1.512	1.530	0.9886	0.3865	0.3895	0.9925
487.1	11.22	11.18	1.003	5.422	5.413	1.002	2.702	2.697	1.002	0.6899	0.6880	1.003
548.0	19.08	18.85	1.012	9.269	9.173	1.010	4.626	4.578	1.010	1.180	1.167	1.011
661.8	32.81	32.89	0.9975	16.05	16.11	0.9959	8.026	8.059	0.9958	2.040	2.051	0.9948
774.8	42.36	42.21	1.003	20.82	20.74	1.003	10.42	10.39	1.003	2.642	2.633	1.004

the spectroradiometer results to a cubic spline and interpolating them to the effective wavelengths of the SXR. Correction was made for a size-of-source effect in the SXR. The results are given in Table 6 as spectral radiance, and the SXR values are divided by the spectroradiometer values. The agreement is within the combined uncertainties of the techniques; however, a degree of consistency in these ratios is evident, as shown in Fig. 7. This indicates a possible error in the absolute calibration because of systematic effects, such as the calibration coefficients for the SXR or the calibration data for the strip lamp.

1.5 CONCLUSIONS

The peak-to-valley variability of the spectral radiance in the exit aperture of the GSFC sphere is between 0.6–0.9% when the sphere is illuminated in a symmetric fashion. When only a single lamp is used, resulting in an asymmetric illumination geometry, these values increase by more than a factor of two. There appears to be no spectral dependence to the variability, and there is a consistent region of lower radiance when compared to the average of the central values. The spectral radiance of the sphere was determined at four different lamp settings using both a prism-grating monochromator from 370–1,100 nm every 10 nm and the SXR at its six fixed wavelengths. The spectral radiance was a smoothly varying function of wavelength, with a peak of 45.21 μW cm^{-2} sr^{-1} nm^{-1} at 890 nm with all 16 lamps operating. The magnitude of the spectral radiance scaled approximately with the number of lamps. The spectral radiances determined by the SXR agreed with those determined by the monochromator and the standard lamp within their combined standard uncertainties.

Acknowledgments

The authors are grateful to Ambler Thompson and Robert Saunders of the Optical Technology Division at NIST for their advice and assistance, and to Charles Gibson who provided a calibrated strip lamp on short notice. This work was supported in part by NASA Interagency Agreement S–64096–E.

Chapter 2

Revised SeaWiFS Prelaunch Algorithm for the Diffuse Attenuation Coefficient $K(490)$

James L. Mueller and Charles C. Trees
Center for Hydro-Optics and Remote Sensing/SDSU
San Diego, California

Abstract

The algorithm relating the diffuse attenuation coefficient $K(490)$ at 490 nm to the ratio of water-leaving radiances $L_W(443)/L_W(555)$ is evaluated through regression analysis of radiometric profiles from oceanographic cruises in the Arabian Sea, Sargasso Sea, the California Current System, the Gulf of California, and the North and South Atlantic Oceans. The resulting algorithm coefficients for this wavelength combination are significantly different, at the 95% confidence level, from those of the CZCS $K(490)$ algorithm based on the ratio $L_W(443)/L_W(550)$. It is recommended, therefore, that the coefficients from the present analysis, rather than those of the CZCS algorithm, be used for the prelaunch SeaWiFS $K(490)$ algorithm.

2.1 INTRODUCTION

The diffuse attenuation coefficient at 490 nm, $K(490)$, was one of the standard ocean data products calculated from Nimbus-7 CZCS imagery. Austin and Petzold (1981) derived the Nimbus-7 CZCS algorithm relating $K(490)$, in per unit meters, to the ratio of water-leaving radiances $L_W(443)/L_W(550)$, at wavelengths of 443 and 550 nm, as

$$K(490) = 0.022 + 0.088\left[\frac{L_W(443)}{L_W(550)}\right]^{-1.491} \text{ m}^{-1}. \quad (5)$$

Root mean square (rms) uncertainties in $K(490)$ estimated from CZCS data are less than 20% (1σ) based on direct comparisons with *in situ* radiometric profiles (e.g., Mueller 1993b).

The SeaWiFS Science Team formally recommended the Austin and Petzold 1981 algorithm, (5), be adopted as the prelaunch $K(490)$ algorithm for SeaWiFS data processing. This algorithm replaces the CZCS water-leaving radiances $L_W(443)$ and $L_W(550)$ with the SeaWiFS *normalized* water-leaving radiances $L_{WN}(443)$ and $L_{WN}(555)$. Some members of the SeaWiFS Science Team, however, questioned whether the shift from 550 to 555 nm might lead to significant systematic errors in SeaWiFS $K(490)$ estimates if the coefficients in (5) are used. Mueller (1995) compared $K(490)$ and $L_{WN}(443)/L_{WN}(555)$ derived from 45 radiometric profiles made during recent cruises using instruments configured with SeaWiFS wavelengths. The profiles that made up this small sample were contributed by:

1) C. Trees (San Diego State University [SDSU] Center for Hydro-Optics and Remote Sensing [CHORS]), 16 profiles from the Arabian Sea;
2) G. Mitchell (University of California San Diego [UCSD] Scripps Institution of Oceanography [SIO]), 18 profiles from the California Current System; and
3) D. Siegel (University of California Santa Barbara [UCSB]), 11 profiles from the Sargasso Sea.

The logarithmic regression analysis of these data resulted in the algorithm

$$\hat{K}(490) = 0.022 + 0.0984\left[\frac{L_{WN}(443)}{L_W(550)}\right]^{-1.403} \text{ m}^{-1}, \quad (6)$$

with a standard error of $0.018\,\text{m}^{-1}$. The coefficients of (5) (Austin and Petzold 1981) fell well within the 90% confidence limits of the coefficients of (6). Mueller (1995) concluded, therefore, that there was insufficient evidence to reject the hypothesis that the two algorithms are equivalent.

During the past year, 242 data triplets [of $K(490)$, $L_{WN}(443)$, and $L_{WN}(555)$] were accrued using radiometric profile data from:

a) Three additional cruises in the Arabian Sea (C. Trees);
b) One cruise in the Gulf of California (E. Valdez, H. Maske, and their colleagues, of *Centro de Investigación Científica y de Educación Superior de Ensenada,* [CICESE] Baja, California, and J. Mueller of CHORS); and

c) The first Atlantic Meridional Transect (AMT-1) of the North and South Atlantic Oceans in September/October 1995 (G. Moore of Plymouth Marine Laboratory [PML], United Kingdom [UK]).

These cruises were carried out, in part, under the SeaWiFS Science Team investigations of the participants. The regression analysis of this larger sample yields algorithm coefficients with much narrower (95%) confidence limits than those associated with (6) (Mueller 1995). In contrast to that earlier result, the new algorithm is significantly different from (5) (Austin and Petzold 1981).

2.2 DATA AND METHODS

Profiles of spectral downwelling irradiance $E_d(z,\lambda)$ and upwelling radiance $L_u(z,\lambda)$ at the SeaWiFS wavelengths (within 2 nm) were obtained from cruises in the:

1) Arabian Sea (C. Trees);
2) California Current System (G. Mitchell);
3) Sargasso Sea near Bermuda and the Joint Global Ocean Flux Study (JGOFS) Bermuda Atlantic Time Series (BATS) site (D. Siegel);
4) Central Gulf of California (J. Mueller, E. Valdez and H. Maske); and
5) North and South Atlantic Oceans, AMT-1 cruise of September–October 1995 (G. Moore).

Table 7 lists the instruments used in conjunction with the profiles taken, in addition to where the instruments were calibrated.

Each calibrated set of profiles of $E_d(z,\lambda)$, $L_u(z,\lambda)$, and $E_s(\lambda)$, as measured with each instrument's deck radiometer, was analyzed using the integral least-squares solution of Mueller (1991) to determine profiles of $K_d(z,\lambda)$ and $K_L(z,\lambda)$, and the vertical attenuation coefficients for $E_d(z,\lambda)$ and $L_u(z,\lambda)$, respectively. The AMT-1 profiles, however, were analyzed by G. Moore at PML. From these profiles, the authors extracted irradiance above the sea surface, $E_s(\lambda)$, and upwelling radiances just below the sea surface, $L_u(0-,\lambda)$, for wavelengths (λ) of 443 and 555 nm. This was, together with remote sensing $K(490)$, calculated by averaging $K_d(z,490)$ over the first optical attenuation length, i.e.,

$$K(490) \;=\; \frac{1}{z_{90}} \int_0^{z_{90}} K_d(z,490)dz, \qquad (7)$$

where z_{90} is the depth and where

$$\frac{E(490,z)}{E(490,0)} \;=\; e^{-\int_0^{z_{90}} K_d(z,490)dz} \;=\; e^{-1} \;=\; 0.37. \qquad (8)$$

Normalized water-leaving radiances $L_{WN}(\lambda)$ for $\lambda \simeq 443$ and 555 nm are calculated as

$$L_{WN}(\lambda) \;=\; L_u(0^-,\lambda) t_f(\lambda) \frac{\overline{F}_0(\lambda)}{E_s(\lambda)}, \qquad (9)$$

where $L_u(0^-,\lambda)$ and $E_s(\lambda)$ are taken from the analyzed profiles, $t_f(\lambda)$ is the upward Fresnel transmittance through the air-sea interface for radiance, and $\overline{F}_0(\lambda)$ is the mean extraterrestrial solar spectral flux. Within less than 1%, $t_f(443)/t_f(555) \simeq 1.0$, so that from (9) the ratio of normalized water-leaving radiances at 443 and 555 nm may be expressed as

$$\frac{L_{WN}(443)}{L_{WN}(555)} \;\simeq\; \frac{L_u(0^-,443)\overline{F}_0(443)E_s(555)}{L_u(0^-,555)\overline{F}_0(555)E_s(443)}. \qquad (10)$$

From the work of Neckel and Labs (1984), $\overline{F}_0(443) = 198.5$ and $\overline{F}_0(555) = 190.0\,\mu\mathrm{W\,cm^{-2}\,nm^{-1}}$.

The logarithmic regression model relating $K(490)$ to the ratio $L_{WN}(443)/L_{WN}(555)$ may be expressed as

$$\ln[K(490) - 0.022] = \ln(A) + B \ln\left[\frac{L_{WN}(443)}{L_{WN}(555)}\right], \qquad (11)$$

where using (5), $A = 0.088$ and $B = -1.491$, or from (6), $A = 0.0984$ and $B = -1.403$. The attenuation coefficient for pure water, $K_w(490) = 0.022\,\mathrm{m^{-1}}$, is the minimum possible value for $K(490)$. The present sample of 242 profile measurements were used to determine best-fit coefficients for (11) using simple linear regression.

2.3 RESULTS

Data from the sample described above were combined, using (10) and (11), to assemble a regression sample of size $N = 242$. The linear least-squares fit to this data is

$$\begin{aligned} \ln\left[\hat{K}(490) - 0.022\right] \;&=\; -2.30261 \\ &-\; 1.29966\; \ln\left[\frac{L_{WN}(443)}{L_{WN}(555)}\right], \end{aligned} \qquad (12)$$

with the multiple correlation coefficient, $R^2 = 0.90$, and a residual standard deviation of 0.293 (in log space). The scatter of these data are illustrated in Fig. 8, together with the best-fit regression line defined by (12). Also shown in Fig. 8, as a dashed line, is (5) (Austin and Petzold 1981).

Equation (12) may be transformed to the form of (5) as

$$\hat{K}(490) \;=\; 0.022 \;+\; 0.1000\left[\frac{L_{WN}(443)}{L_{WN}(555)}\right]^{-1.300} \mathrm{m^{-1}}. \qquad (13)$$

The measured data pairs are compared to (13) in Fig. 9 [$L_{WN}(443)/L_{WN}(555)$ on a logarithmic scale compared to linear $K(490)$].

The linear residual standard deviation of $\hat{K}(490)$ (*standard error of the estimate*) associated with (13) is

$$\begin{aligned} S_{\mathrm{Kx}} \;&=\; \left[\frac{\sum_{n=1}^{N}\left[\hat{K}_n(490) - K_n(490)\right]^2}{N-2}\right]^{1/2} \\ &=\; 0.017\,\mathrm{m^{-1}}, \end{aligned} \qquad (14)$$

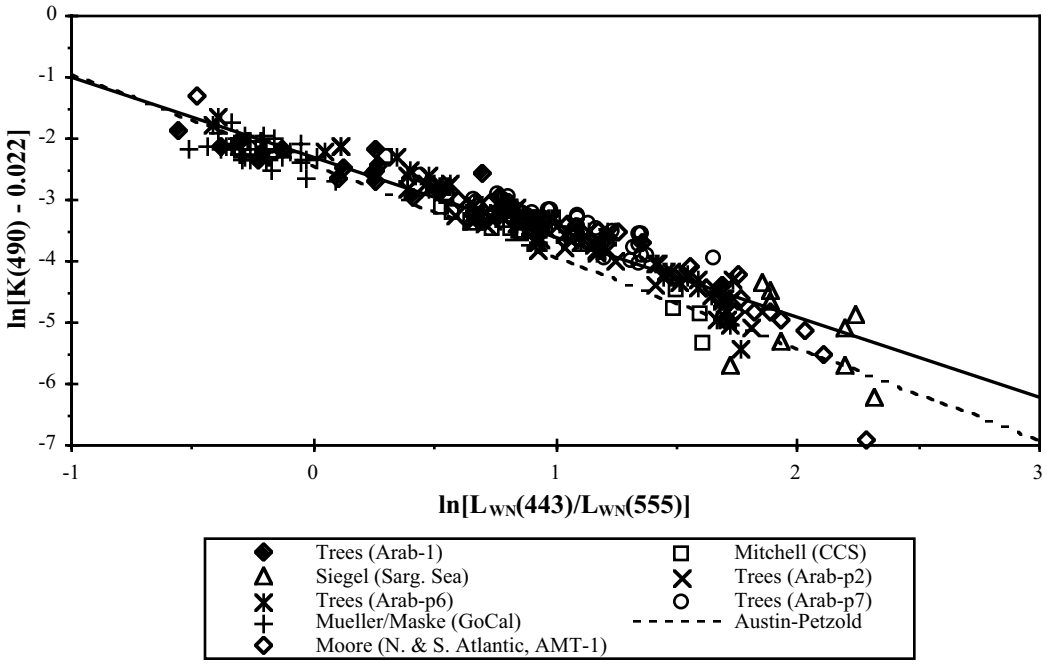

Fig. 8. Scattergram comparing $K(490)$ and the normalized ratio $L_{WN}(443)/L_{WN}(555)$ from the Arabian Sea, California Current System (CCS), Sargasso Sea, Gulf of California (GoCal), and the North and South Atlantic (AMT-1). The solid line is the least-squares fit to the data, and the dashed line illustrates the CZCS $K(490)$ algorithm of Austin and Petzold (1981). The resulting regression equation is $\ln\left[\hat{K}(490)-0.022\right] = -2.30261-1.29966\ln\left[L_{WN}(443)/L_{WN}(555)\right]$ with $R^2 = 0.90$; and the standard error of the estimate is $\sigma = 0.017\,\mathrm{m}^{-1}$.

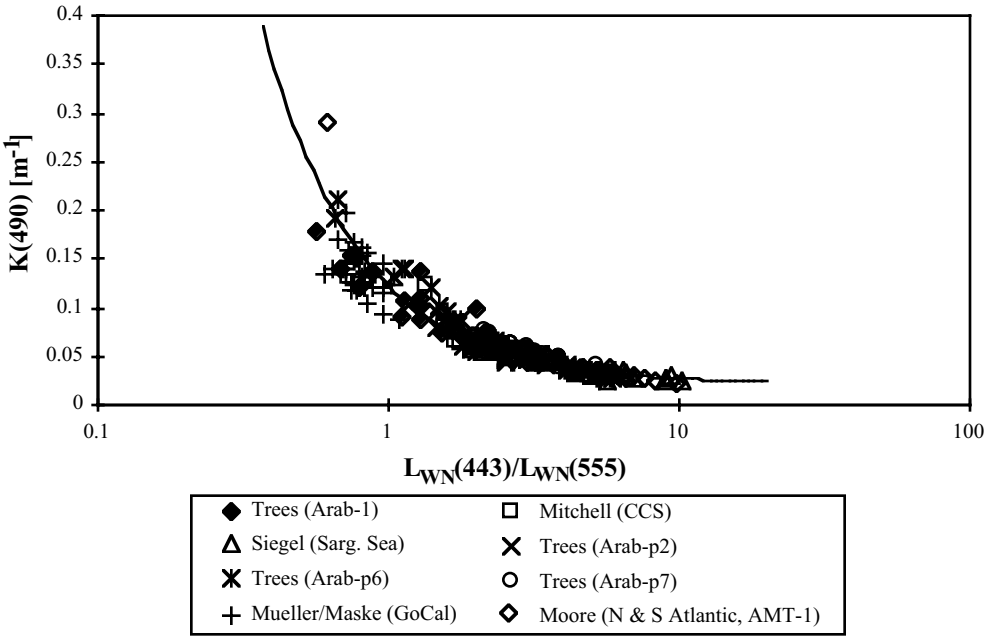

Fig. 9. Linear $K(490)$ versus a logarithmic scaling $L_{WN}(443)/L_{WN}(555)$ display of the data and regression fit (solid curve) from Fig. 8.

Table 7. This table lists the instruments used, as well as where the instruments were calibrated, for their respective set of profiles.

Profiles	*Instruments Used*	*Calibration Site*
Arabian Sea	MER-1032† MER-2040†	CHORS
California Current System	MER-2040†	CHORS BII†
Sargasso Sea	MER-2040†	UCSB
Gulf of California	PRR-600	CHORS
North and South Atlantic Oceans (AMT-1)	OCI-200	PML

† All four MER instruments were manufactured by Biospherical Instruments, Inc. (BII), of San Diego, California.

and the fit is unbiased. When (5) is applied to this data set, the linear residual standard deviation (in this case the *standard error of prediction*) $S_{\mathrm{Kx}} = 0.018\,\mathrm{m}^{-1}$, and the mean linear bias of the Austin and Petzold (1981) estimates of $\hat{K}(490)$, is $-0.007\,\mathrm{m}^{-1}$.

The (upper, lower) 95% confidence limits of the intercept in (12) are (−2.27452, −2.36003), and the 95% confidence limits of the slope are (−1.24596, −1.35335). Both the intercept (−2.4303) and slope (−1.491) of the natural log-transform of (5) fall outside these limits. On this basis, there is sufficient evidence at the 95% confidence level to reject the hypothesis that (5) is equivalent to (13).

2.4 DISCUSSION

Figures 8 and 9 emphasize scatter at different levels of $K(490)$. In the log-log display of Fig. 8, the largest deviations from the regression fit occur at low values of $K(490)$, within less than $0.01\,\mathrm{m}^{-1}$ of pure water. When the $K(490)$ data are displayed on a linear axis (Fig. 9), it is immediately apparent that these deviations at low $K(490)$, which appear to be very large in Fig. 8, are actually very small discrepancies. In fact, the linear $K(490)$ scale (Fig. 9) clearly shows that the largest contributors to the linear standard error of the estimate, S_{Kx}, (14), are at the high values [$K(490) \gtrsim 0.1$].

The analysis outlined in this paper addressed the question of whether the Austin and Petzold (1981) $K(490)$ algorithm, (5), which is based on the $L_W(443)/L_W(550)$ ratio, will produce accurate $K(490)$ estimates when it is used with the $L_{WN}(443)/L_{WN}(555)$ ratio. The log-transformed coefficients of (5) fall outside the 95% confidence limits of the coefficients of (12), the log-linear least-squares fit to the present sample of 242 [$K(490)$, $L_{WN}(443)/L_{WN}(555)$] pairs. Therefore, there is sufficient evidence at the 95% confidence level to reject the hypothesis that (5) is equivalent to (13). The difference between the two sets of predictions, while small, is nevertheless statistically significant at the 95% confidence level. Changing this algorithm's coefficients, therefore, will improve the statistical uncertainty associated with the SeaWiFS $K(490)$ at-launch products. This change should be simple to implement, and the authors recommend that it be done.

In closing, note that the normalized water-leaving radiances used here were not corrected for either instrument self shading, or the ocean bidirectional reflectance distribution function (Morel and Gentili 1996). Furthermore, the $E_d(490, z)$ profiles from which $K(490)$ values were determined were not corrected for Raman scattering. These corrections, which are assumed to be small, are deferred for possible use in a postlaunch refinement of this SeaWiFS algorithm.

Chapter 3

A Simplified Out-of-Band Correction Algorithm for SeaWiFS

Eueng-nan Yeh
Robert A. Barnes
General Sciences Corporation
Laurel, Maryland

Abstract

The SeaWiFS instrument will scan through a broad area of known radiance, and the measurement for each band may contain signals from outside of the desired bandwidth. A calculation that will quickly remove the out-of-band contamination is presented here.

3.1 INTRODUCTION

SeaWiFS is an eight-band filter radiometer. For SeaWiFS, as well as for other satellite instruments managed at GSFC, the spectral response of the instrument is divided into in-band and out-of-band responses. The in-band response includes the wavelength region where the response of the band is greater than 1% of the maximum response; at all other wavelengths, the response is out-of-band.

For each SeaWiFS band, the out-of-band response is within the specification for the instrument (Barnes et al. 1994a). These out-of-band responses, however, must be accommodated in the data reduction algorithms for on-orbit SeaWiFS measurements. The original out-of-band correction algorithm was derived for measurements by SeaWiFS from a radiant source with the spectral shape of a 5,900 K blackbody (Barnes et al. 1994b). This is the reference source spectral shape in the SeaWiFS performance specifications (Barnes et al. 1994a). Subsequently, an out-of-band correction scheme was developed that uses SeaWiFS measurements to determine the spectral shape of the upwelling Earth radiances which SeaWiFS measures (Barnes et al. 1995). Although this correction technique gives accurate out-of-band responses, the technique requires an algorithm that uses a great deal of computation time. As a result, Barnes et al. (1996) derived an alternate approach that produces out-of-band calculations much faster in terms of computer time. The equations in Barnes et al. (1996) are the basis for the computer code presented here. A benchmark test of 200 SeaWiFS scan lines has shown that the new algorithm operates about 120 times faster than its predecessor. In addition, the benchmark test showed the calculated results from the two algorithms to be equivalent at the 0.1% level.

3.2 THE `out_bandsub` ALGORITHM

Prior to the application of atmospheric correction to derive geophysical values, the level-1 radiances from SeaWiFS need an out-of-band correction. The corrections for out-of-band response range from about 0.5% to more than 5%. The level-1 data correction routine, `out_bandsub`, takes an array of calibrated level-1b radiances and, after applying the out-of-band correction, returns a corresponding array of corrected level-1b data. This subroutine is designed to work one scan line with eight bands at a time. This procedure is written in C.

The input arguments for this algorithm are:

1) `rad` (real number, array size 8×1285): the level-1b radiances (bands 1–8) per line;
2) `oxygen` (real number): the oxygen absorption correction factor; equals 1 if `rad`(76 nm) is already corrected, otherwise it equals 1.12;
3) `xsample` (integer): number of pixels per line (maximum of 1,285).

There is only one output argument, which is:

`rad` (real number, array size 8×1285): the level-1b out-of-band corrected radiances (bands 1–8).

This simplified out-of-band method applies the ratio of in-band response to the total band response as an out-of-band correction factor (k_b, Table 11, Barnes et al. [1996]) for each band. This process will go through each pixel of a line:

```
for (m = 0; m < xsample; m++) \{
   original_input_8 = rad[7][m];
   original_input_6 = rad[5][m];
   original_input_5 = rad[4][m];
   for (n = 0; n < 8; n++) rad[n][m] *= Kb[n];.
```

Before bands 8, 6, and 5 can be further revised, the oxygen absorption effect and radiance at 765 nm should be established:

```
XOUT = rad[6][m] * oxygen;
OUT9 = 2 * rad[7][m] - XOUT;.
```

The simplified out-of-band calculation of SeaWiFS band 8 divides the spectral response, based on a spectrally flat source, into six components (Fig. 20, Barnes et al. [1996]). These response values, S, are listed in Table 13 of Barnes et al. (1996); thus, for a given pixel the new k_b of band 8 is

```
XN = rad[7][m] * S[4];
XD = rad[0][m]*S[0] + rad[3][m]*S[1] + rad[4][m]*S[2]
   + XOUT*S[3] + XN + OUT9*S[5];
NEW_Kb = XN / XD;
```

and the final result for band 8 is

```
rad[7][m] = NEW_Kb * original_input_8;.
```

The correction calculations for band 6 is a simplified version of that for band 8. The spectral response, S, is divided into three components (Table 14, Barnes et al. [1996]). The revised k_b of band 6 is

```
XN = rad[5][m] * S[1];
XD = rad[2][m]*S[0] + XN + rad[7][m]*S[2];
NEW_Kb = XN / XD;
```

and the final result for band 6 is

```
rad[5][m] = NEW_Kb * original_input_6;.
```

Similarly, the three components of the band 5 spectral response, S, are listed in Table 15 of Barnes et al. (1996). The revised k_b of band 5 is

```
XN = rad[4][m] * S[1];
XD = rad[1][m]*S[0] + XN + rad[5][m]*S[2];
NEW_Kb = XN / XD;
```

and the final result for band 5 is

```
rad[4][m] = NEW_Kb * original_input_5;
  }.
```

Chapter 4

SeaWiFS Stray Light Correction Algorithm

Eueng-nan Yeh and Michael Darzi
General Sciences Corporation
Laurel, Maryland

Lakshmi Kumar
Hughes STX
Lanham, Maryland

Abstract

SeaWiFS will scan through not only the dark ocean surface, but also the bright land, clouds, and ice objects. Because of stray light in the SeaWiFS instrument, light from these bright sources can contaminate ocean measurements several pixels away from a bright source. A mathematical formula that can be used to correct this contamination is discussed here.

4.1 INTRODUCTION

Two routines were developed, `stray_light_lac` and `stray_light_gac`, to apply a stray light correction to SeaWiFS level-1 LAC and GAC data, respectively. The routines are integrated as part of the operational level-1a read routine; their algorithms are based on the methodology described by Barnes et al. (1995). The routines perform radiance manipulations to label pixels that are bright sources or are in the vicinity of bright sources. In addition, the radiances of pixels that are along scan to, and near, a bright source are corrected for stray light contamination from that bright source. Because the input data to the routines are radiances, the calibrated level-1 data, i.e., level-1b data, must be used.

The labelling identifies pixels that are part of a bright source, near a bright source in the along-track direction, diagonal to the ends of a bright source, or near a bright source in the along-scan direction. These along-scan pixels are correctable for stray light contamination as a function of their distance from the bright source. For this reason, they are labelled by their pixel distance from the nearest edge of a bright source to the right of that pixel and from the nearest edge of a bright source to the left of that pixel. For LAC, 14 pixels to the left and 12 pixels to the right of a bright source edge are considered to be affected by stray light from that bright source. For GAC, 3 pixels on each side of a bright source are so considered. If a stray light pixel is within this range between two bright sources, the pixel distance to the bright source on the right is multiplied by 1,000; the product is then added to the pixel distance to the bright source on the left.

Both routines are designed to work on individual scan lines even though along-track processing is required. This is accomplished by using a buffer that retains a rolling window of consecutive scan lines.

4.2 LAC CORRECTION

There are two major steps involving the SeaWiFS LAC image stray light correction for level-1b data (Fig. 10). The first step is to identify the left and right bright source edges. Two conditions, radiance value and gradient value, are applied to SeaWiFS level-1 band 8 (865 nm) radiance ($L8$) to identify these edges. The radiance of a pixel has to exceed a certain threshold, `Stray_thresh`, which is defined as a fraction of the value of $L8$ at knee 1. The value of the typical stray light fraction, `Styp_frac`, is given as 0.9. The radiance gradient, Δ_L, is defined as the $L8$ difference between two adjacent pixels $n+1$ and n. The left edge is found if the radiance value is greater than `Stray_thresh` and Δ_L is greater than the typical gradient threshold value. This value is defined as a fraction of the bigger one of the following two quantities: $L_{\text{typical}}(8)$, or the difference between $L8$ of pixel $n+1$, i.e., $L8[n+1]$, and $L_{\text{typical}}(8)$. The $L_{\text{typical}}(8)$ is the typical quantity of sea surface radiance measured by band 8 and the value is $1.09\,\text{mW}\,\text{cm}^{-2}\,\mu\text{m}^{-1}\,\text{sr}^{-1}$. The radiance fraction `Ltyp_frac` is given as 0.25. The right edge is found if the radiance value is greater than `Stray_thresh` and Δ_L is greater than the typical gradient threshold value, which is defined as a fraction of the bigger one of the following two quantities: $L_{\text{typical}}(8)$, or the difference between $L8$ of pixel n, i.e., $L8[n]$, and $L_{\text{typical}}(8)$.

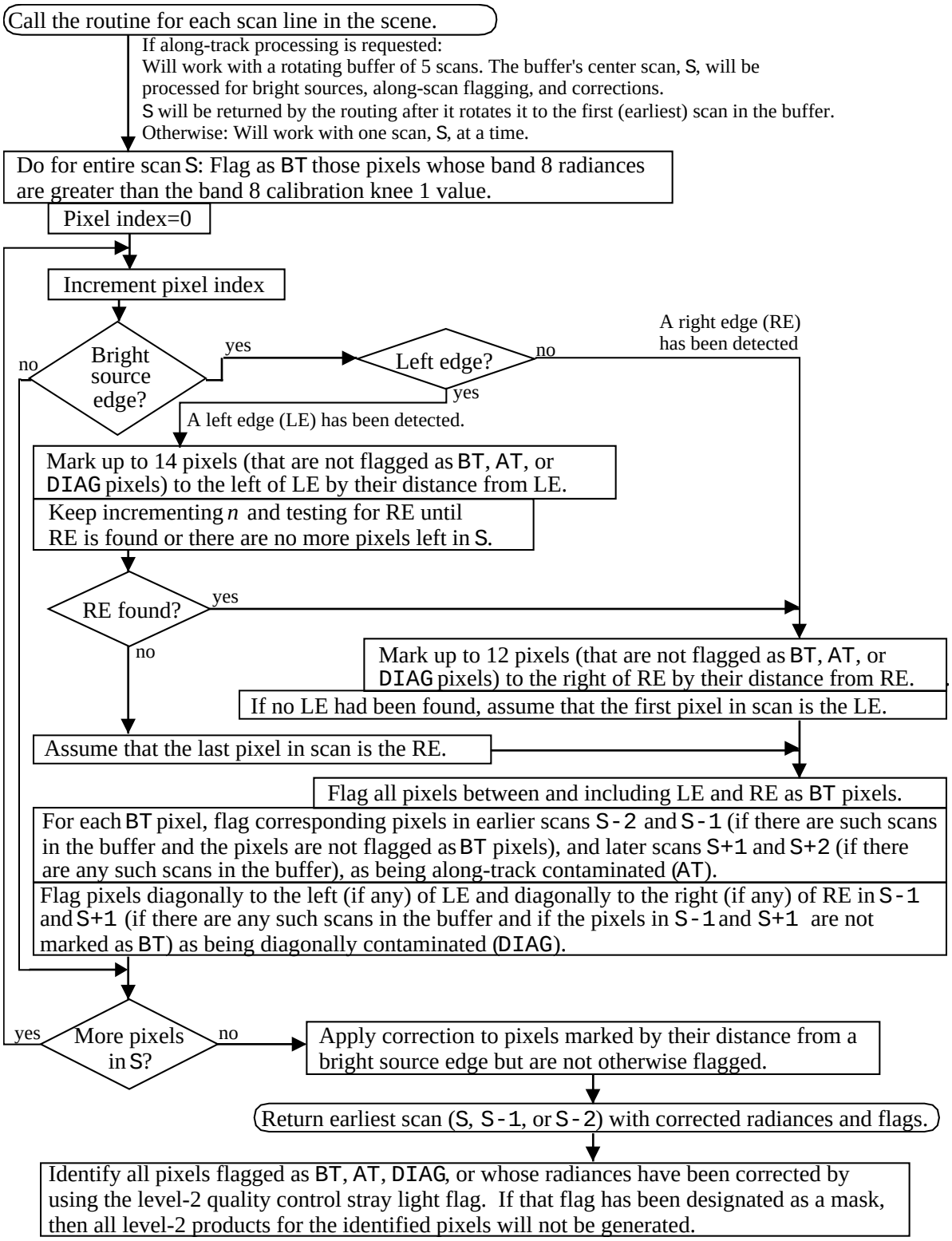

Fig. 10. A logic flow diagram for the detection and correction of stray light in SeaWiFS LAC level-1 data is shown.

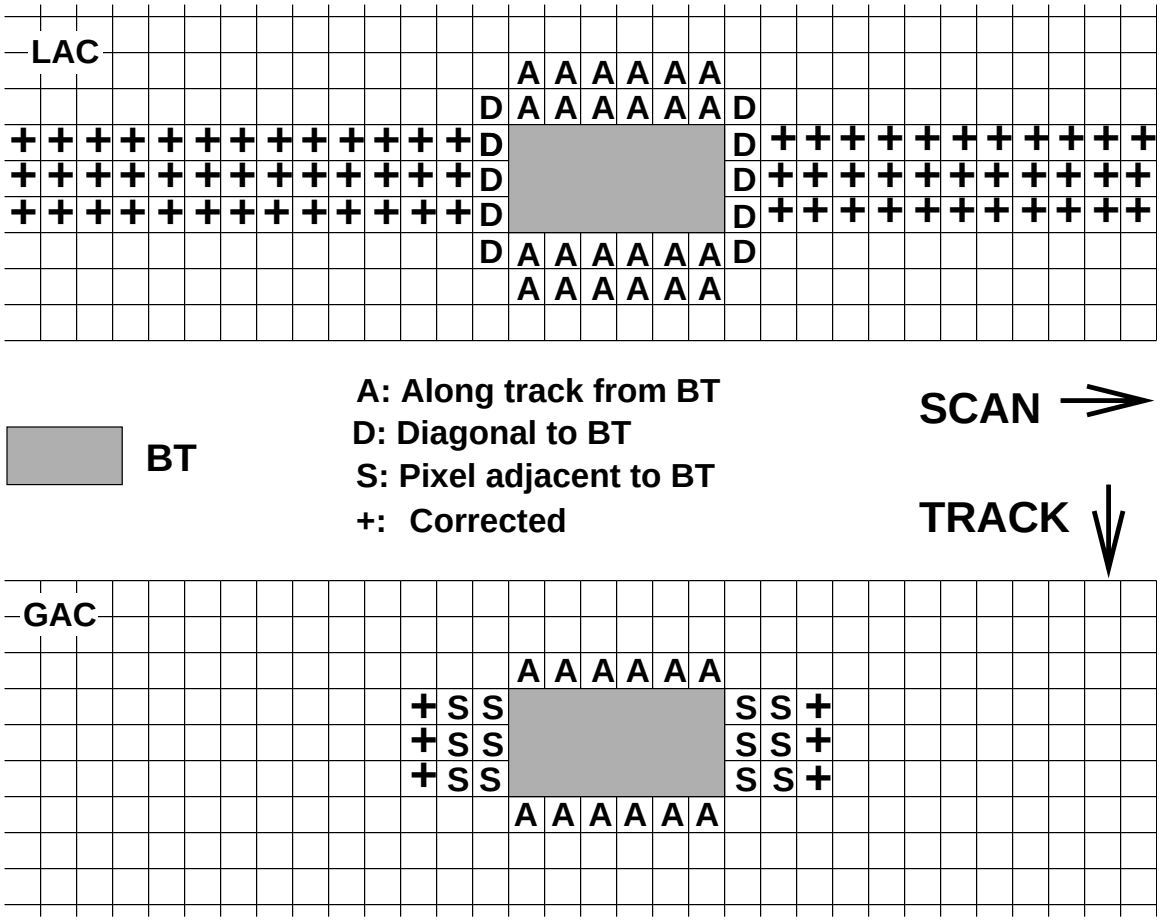

Fig. 11. This is a schematic illustration of how the stray light correction is done for LAC and GAC scenes. The arrow of `SCAN` indicates the instrument scanning direction. The arrow of `TRACK` indicates the direction of satellite movement. The shaded area represents the bright source region. Symbols `A`, `D`, and `S` represent flags for along-track from, diagonal to, and the scan adjacent to the bright source, respectively. The + sign represents a stray light corrected pixel. These pixels are also flagged as the distance from the bright source edge.

The second step is to mask and correct the bright source affected pixels (Fig. 11). All pixels between the left and right bright source edges will be flagged as a bright target (`BT`) for subsequent masking by the SeaWiFS processing program. In addition, 14 `LRANGE` (extra pixels to the left), and 12 `RRANGE` (extra pixels to the right of bright source edges) will be flagged by their distances from their respective bright source edge as stray-light contaminated pixels if they have not been flagged as `BT`, along-track (`AT`), or diagonal (`DIAG`) pixels before. These pixels will later be corrected by the along-scan direction correction algorithm for the contamination. If along-track masking is selected, all pixels not identified as `BT`s between the left and right bright source edges on the previous two lines and next two lines will be flagged as along-track pixels. Only one extra pixel to the left and one extra pixel to the right of bright source edges of one previous line and one subsequent line will be flagged as diagonal pixels.

The along-scan direction stray light correction ($L_{\rm corr}$) for pixel 0 proceeds in the following sequence:

Sequence 1, set the correction term to zero:

$$L_{\rm corr} \;=\; 0. \tag{15}$$

Sequence 2, replace pixel 0 radiance, $L[0]$, as:

$$L_{\rm corr} \;=\; L_{\rm corr} \;+\; L[0](1 \;-\; K[0]), \tag{16}$$

where $K[0]$ is the stray light correction constant for pixel 0. The values of K are listed in Table 8.

Sequence 3, remove the stray light contributions from the adjacent pixels:

$$L_{\rm corr} \;=\; L_{\rm corr} \;-\; L[-1]K[+1], \tag{17}$$

$$L_{\rm corr} \;=\; L_{\rm corr} \;-\; L[-2]K[+2], \tag{18}$$

$$L_{\rm corr} \;=\; L_{\rm corr} \;-\; L[+1]K[-1], \tag{19}$$

Table 8. Along-scan responses for SeaWiFS bands 1–8 with their respective wavelengths, in nanometers, in parentheses. These are the constants, K, used in the LAC stray light correction procedure.

Pixel	*Band Numbers and Wavelengths* [nm]							
Offset	1 (412)	2 (443)	3 (490)	4 (510)	5 (555)	6 (670)	7 (765)	8 (865)
−12	0.00000	0.00005	0.00000	0.00006	0.00000	0.00005	0.00000	0.00003
−11	0.00000	0.00014	0.00000	0.00020	0.00000	0.00016	0.00000	0.00010
−10	0.00000	0.00029	0.00000	0.00034	0.00000	0.00027	0.00000	0.00016
−9	0.00000	0.00048	0.00000	0.00052	0.00000	0.00048	0.00000	0.00026
−8	0.00004	0.00071	0.00004	0.00070	0.00002	0.00076	0.00000	0.00039
−7	0.00010	0.00086	0.00010	0.00078	0.00005	0.00098	0.00003	0.00048
−6	0.00030	0.00105	0.00025	0.00090	0.00015	0.00129	0.00010	0.00064
−5	0.00080	0.00124	0.00073	0.00104	0.00045	0.00140	0.00031	0.00086
−4	0.00240	0.00141	0.00195	0.00157	0.00135	0.00168	0.00096	0.00118
−3	0.00639	0.00494	0.00534	0.00444	0.00343	0.00292	0.00232	0.00239
−2	0.01757	0.01271	0.01531	0.01044	0.00925	0.00599	0.00758	0.00710
−1	0.13172	0.09747	0.21432	0.10994	0.06548	0.05577	0.18735	0.23668
0	0.73254	0.83142	0.73217	0.86085	0.67127	0.70802	0.67749	0.66297
1	0.06387	−0.00424	−0.00267	−0.00104	0.23406	0.19771	0.09616	0.05512
2	0.01998	0.03237	0.01956	−0.00418	0.00737	0.01381	0.01971	0.01586
3	0.01038	0.01271	0.00607	0.00914	0.00298	0.00550	0.00372	0.00796
4	0.00350	0.00419	0.00176	0.00301	0.00150	0.00194	0.00133	0.00382
5	0.00300	0.00141	0.00146	0.00090	0.00059	0.00081	0.00079	0.00191
6	0.00230	0.00052	0.00108	0.00026	0.00052	0.00030	0.00061	0.00089
7	0.00200	0.00019	0.00083	0.00008	0.00045	0.00011	0.00044	0.00048
8	0.00140	0.00007	0.00065	0.00003	0.00035	0.00004	0.00031	0.00029
9	0.00110	0.00002	0.00049	0.00000	0.00030	0.00002	0.00028	0.00016
10	0.00050	0.00000	0.00031	0.00000	0.00022	0.00000	0.00021	0.00010
11	0.00013	0.00000	0.00020	0.00000	0.00015	0.00000	0.00014	0.00010
12	0.00000	0.00000	0.00007	0.00000	0.00007	0.00000	0.00010	0.00006
13	0.00000	0.00000	0.00000	0.00000	0.00000	0.00000	0.00007	0.00003
14	0.00000	0.00000	0.00000	0.00000	0.00000	0.00000	0.00003	0.00000

and

$$L_{\text{corr}} \;=\; L_{\text{corr}} \;-\; L[+2]K[-2], \tag{20}$$

until pixels `LRANGE` (equals 14) and `RRANGE` (equals 12) are reached.

Sequence 4, correct the radiance:

$$L[0] \;= L[0] \;+\; L_{\text{corr}}. \tag{21}$$

The above sequences are applied to all eight SeaWiFS bands.

This subroutine is designed to work one scan line with eight bands at a time; this procedure is written in C.

The variables, both for input and output, needed for the function `stray_light_lac` are summarized in Table 9.

This subroutine, `stray_light_lac`, calls for each scan line in the scene:

```
status = stray_light_lac(initial, Ltyp_frac,
         Styp_frac, nscans, nsamples, scan_no,
         gn, rads, l1b_data, sl_scan, sl_flag).
```

If along-track processing is requested, this subroutine will use a rotating buffer of five scans to mark as `BT` and along-scan flagging and corrections on the current scan line, `S`. Other scans in the buffer will store information of pixels flagged with `AT` and `DIAG`. Otherwise, it will work with one scan, `S`, at a time.

As discussed in previous sections, the stray light algorithm will try to identify stray light affected pixels and correct them if possible. The first step to find stray light pixels is to screen through each pixel, from scan `S`, and verify if it is a bright source pixel. The test is if $L8$ is greater than the knee value, then set the flag buffer as `BT`. Table 10 is the first knee value of band 8, which will be used for `Stray_thresh` value calculation. This screening can speed up the determination of bright source edges, which will skip consecutive bright source pixels.

The bright source edges can be identified by tests of two quantities: radiance value and gradient value. The edge is a left edge if the gradient shows a positive value. A negative gradient means a right bright source edge is detected. The flag buffer will mark up to `LRANGE` or `RRANGE` pixels to the left or right of bright source edges by their

Table 9. Listed below are the LAC input and output parameters.

Variable	*Data Type*	*Variable Description*
		Input Parameters
`initial`	*int32*	Should be set to 1 for the first call of a scene.
`Ltyp_frac`	*float32*	Fraction (=0.25) factor of L_{typical} to determine the bright target edge.
`Styp_frac`	*float32*	Fraction (=0.90) factor of band 8 knee 1 radiance to determine the bright target edge.
`nscans`	*int32*	This is the processing indicator. If `nscans=1`, it will perform only along-scan direction stray light correction processing. If `nscans=maximum` of the file records, it will do both along-scan and along-track stray light processing.
`nsamples`	*int32*	Number of pixels per line.
`scan_no`	*int32*	Scan line number (0-relative) of input data.
`gn`	*int16*	Band 8 gain of scan line `scan_no`.
`rads`	*float32*	Knee radiance values [8×4×5].
`l1b_data`	*float32*	An array of `nsamples` long containing `l1b_data` (8 bands) of scan line `scan_no`.
		Output Parameters
`l1b_data`	*float32*	An array of stray light corrected level-1b data.
`sl_scan`	*int32*	Scan line number for which the returned `l1b_data` is applied.
`sl_flag`	*int32*	An array of `nsamples` long containing codes identifying bright target pixels and the proximity of others to bright targets. The meaning of `sl_flag` value is: 0 A bright target flag (`BT`); −1 An along-track flag (`AT`); −2 A diagonal flag (`DIAG`); >0 The number represents the distance in pixels away from the bright target edges—if a pixel is within range of two bright targets, `sl_flag` will equal the pixel distance from the left bright target edge plus 1,000 times the pixel distance from the right bright target edge (a `sl_flag` value of 3001 means three pixels away from the bright target edge on the right and one pixel away from left bright target edge); and −10 None of the above (`BLANK`).
Return value	*int32*	Returns as 0, *not done*, to indicate that the routine did not return any useful information for the last call, but was filling its buffers with scan line data; and 1, *done*, to indicate that the `l1b_data` and `sl_flag` arrays for scan line `sl_scan` have been set.

Table 10. These are the band 8 knee 1 values for the SeaWiFS bilinear gains. The radiances are in units of $\text{cm}^{-2}\,\text{sr}^{-1}\,\mu\text{m}^{-1}$.

Gain	*1*	*2*	*3*	*4*
Knee Radiance	1.64928	0.830554	6.32555	3.30217
Knee Count	762.30	758.12	794.66	773.58

distance from the respective edge, assuming these pixels have not been flagged as `BT`, `AT`, or `DIAG` pixels.

For a pixel within the range of two bright sources, the flag buffer will mark the distance as the sum of the pixel distance from the left bright source edge plus 1,000 times the pixel distance from the right bright source edge. Pixels with flag buffers marked as *distance* will eventually perform the along-scan stray light correction. If a left and right edge pair fails to identify one of the two edges, the first pixel in scan `S` will be assigned as the beginning of the left edge for the missing left edge, or the last pixel in `S` will be assigned as the ending of the right edge for the missing right edge.

The flag buffer will mark all pixels between, and including, the left and right edges as `BT` pixels for scan `S`. If along-track masking is the option, for each `BT` pixel, the

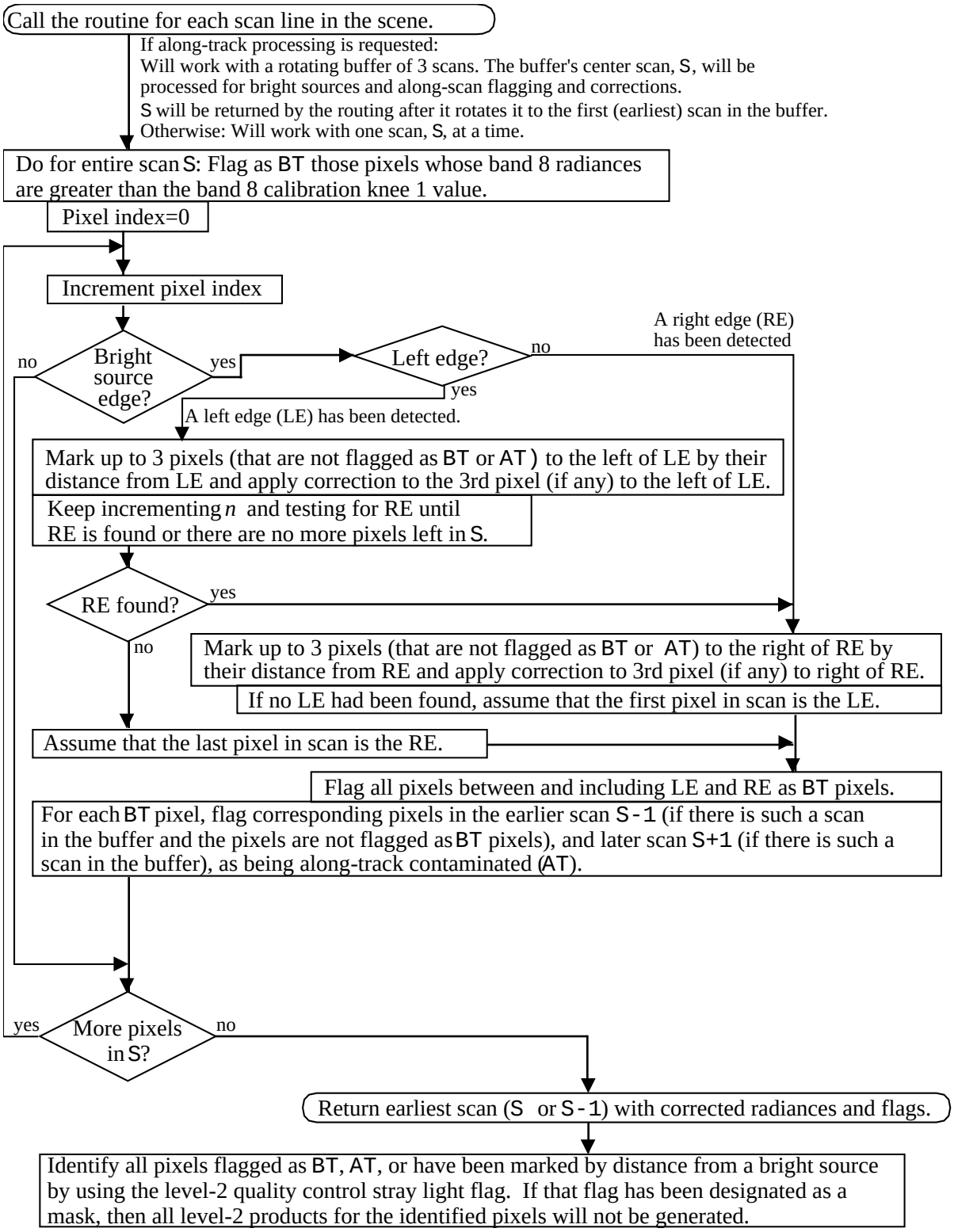

Fig. 12. Logic flow diagram for the detection and correction of stray light in SeaWiFS GAC level-1 data.

Table 11. Along-scan GAC stray light correction factors, K.

Band Number	*Pixels Before Bright Source*			*Pixels After Bright Source*		
	−1	−2	−3	1	2	3
1	−0.00000	0	0	0	0	−0.00090
2	−0.00060	0	0	0	0	−0.00001
3	−0.00000	0	0	0	0	−0.00055
4	−0.00074	0	0	0	0	−0.00000
5	−0.00000	0	0	0	0	−0.00053
6	−0.00055	0	0	0	0	−0.00000
7	−0.00000	0	0	0	0	−0.00055
8	−0.00037	0	0	0	0	−0.00033

corresponding pixel in earlier scans (`S-1` and `S-2`) and later scans (`S+1` and `S+2`) will be flagged as `AT` for stray light contaminated pixels, assuming the scan lines do exist and the pixels have not been marked as `BT`. The flag buffer will also mark one extra pixel to the left or right of the left or right edge on scans `S-1` and `S+1` as `DIAG` for stray light contaminated pixels, assuming the scan lines do exist and the pixels have not been marked as `BT`. The bright source edge detection and flag buffer flagging will run through the whole scan `S`. The along-scan direction stray light correction algorithm will apply to the pixel, having the distance as the flag indicator.

This program will output the earliest scan (`S-2`, `S-1`, or `S`) with stray light corrected radiances and flags. The information contained in the flag record can be used to identify all pixels flagged as `BT`, `AT`, `DIAG`, or the distance from a `BT` edge. If that flag has been designated as a mask, then all level-2 products for the identified pixels will not be generated.

4.3 GAC CORRECTION

The algorithm for GAC stray light correction, identifying bright sources and edges, is similar to that for the LAC correction algorithm (Fig. 12). The GAC along-scan correction, however, is applied only to the third GAC pixel from the bright source edge:

$$L[3] \;=\; L[3] \;+\; L_{\text{edge}}K[3], \tag{22}$$

where $L[3]$ represents the level-1 radiance at three pixels away from the bright source edge. K is the GAC stray light correction constant and its value is listed in Table 11. The above equation is also applied to all eight SeaWiFS bands.

The GAC stray light correction algorithm will flag three pixels before the left edge and three pixels after the right edge (by their distances from respective bright source edges) as stray light contaminated pixels if they have not been previously flagged as `BT` or `AT` pixels.

The parameters used for the `stray_light_gac` function are similar to that of the `stray_light_lac` function (Table 9). The only exception is that `GAC` does not have `DIAG` flags.

Unlike LAC, the GAC rotating buffer contains only three scan lines if along-track processing is requested and the output will be the earliest scan (`S-1`, or `S`). The flag buffers will not contain `DIAG` flags. The value of `LRANGE` and `RRANGE` is 3 with only the third GAC pixel from the bright source edge corrected for stray light contamination. Other than that, the GAC software is the same as the LAC software.

4.4 STRAY LIGHT MASKING

As mentioned before, the stray light affected pixels will be flagged as bright source (`BT` = 0), along track (`AT` = −1), diagonal (`DIAG` = −2), or distance (greater than or equal to 1, in units of pixels) away from the bright source edges. The distance range for a LAC scene can be 14 pixels to the left of a bright source left edge and 12 pixels to the right of a bright source right edge. All pixels with positive flag settings will be corrected for stray light contaminations. As a GAC scene, however, the distance range will go up to only three pixels on both sides of bright source edges and only the third pixel will be corrected. All pixels not affected by stray light will be flagged as blank (`BLANK` = −10).

Further analysis of the flag output, `sl_flag`, will reset the flag values between −10 (exclude) and the value of the maximum distance range of 256, i.e., the SeaWiFS level-2 stray light masking. In this way, the pixels with corrections will also be masked out.

Glossary

AMT Atlantic Meridional Transect
ASCII American Standard Code for Information Interchange
AVHRR Advanced Very High Resolution Radiometer

BATS Bermuda Atlantic Time Series
BII Biospherical Instruments, Inc.

CCS California Current System
CHORS Center for Hydro-Optics and Remote Sensing
CICESE *Centro de Investigación Científica y de Educación Superior de Ensenada* (Baja, California)
CVT Calibration and Validation Team
CZCS Coastal Zone Color Scanner

DC Direct Current

EOSDIS Earth Observing System Data and Information System

FASCAL Facility for Automated Spectroradiometric Calibrations

GAC Global Area Coverage
GoCal Gulf of California
GOES Geostationary Operational Environmental Satellite
GSFC Goddard Space Flight Center

HP Hewlett-Packard

IEEE Institute of Electrical and Electronic Engineers
ISIC Integrating Sphere Irradiance Collector

JGOFS Joint Global Ocean Flux Study

LAC Local Area Coverage
LANDSAT Land Resources Satellite
LE Left Edge

MER Marine Environmental Radiometer

NASA National Aeronautics and Space Administration
NIST National Institute of Standards and Technology
NOAA National Oceanic and Atmospheric Administration

OSC Orbital Sciences Corporation

PC Personal Computer (IBM)
PML Plymouth Marine Laboratory
PSR Point Spread Response

RE Right Edge
rms root mean square

SBRS (Hughes) Santa Barbara Remote Sensing
SDSU San Diego State University
SeaWiFS Sea-viewing Wide Field-of-view Sensor
SIO Scripps Institution of Oceanography
SIRREX SeaWiFS Intercalibration Round-Robin Experiment
SIRREX-1 The First SIRREX (July 1992)
SIRREX-2 The Second SIRREX (June 1993)
SIRREX-3 The Third SIRREX (September 1994)
SIRREX-4 The Fourth SIRREX (May 1995)
SRR Spectral Radiance Responsivity
SXR SeaWiFS Transfer Radiometer

UCSD University of California, San Diego
UCSB University of California, Santa Barbara
UK United Kingdom

VISSR Visible-Infrared Spin-Scan Radiometer

Symbols

A Logarithmic regression model coefficient.

B Logarithmic regression model coefficient.

$E_d(z,\lambda)$ Downwelling irradiance.
$E_s(\lambda)$ Downwelling irradiance incident at the sea surface.

$\overline{F}_0(\lambda)$ Mean extraterrestrial solar flux.

I Current.

$k_{\rm b}$ Out-of-band correction factor.
K Stray light correction constant.
$K(490)$ Remote sensing diffuse attenuation coefficient, in per unit meters. The average of $K_d(z,490)$ over the first attenuation length.
$\hat{K}(490)$ Regression model estimate of $K(490)$ in per unit meters.
$K_d(z,\lambda)$ Vertical attenuation coefficient for $E_d(z,\lambda)$, in per unit meters.
$K_L(z,\lambda)$ Vertical attenuation coefficient for $L_u(z,\lambda)$, in per unit meters.
K_w Attenuation coefficient for pure water.

L Spectral radiance.
$\hat{L}$ The spectral radiance from a calibrated (known) source.
$\tilde{L}$ The spectral radiance from a measured (unknown) source.
$L8$ Level-1 band 8 radiance.
$L_{\rm corr}$ Along-scan radiance correction factor.
L_G Spectral radiance measured with a gas filled strip-lamp standard.
L_S Spectral radiance measured with a spectroradiometer.
$L_{\rm typical}(8)$ Typical quantity of sea surface radiance measured by band 8.
$L_u(z,\lambda)$ Upwelling spectral radiance at depth z.
L_W Water-leaving radiance.
$L_{WN}(\lambda)$ Normalized water-leaving radiance at the top of the sea surface ($z = 0+$).

N Sample size.

R Spectral radiance responsivity.
R^2 Multiple correlation coefficient.

S Response value.
$\hat{S}$ The signal from a calibrated (known) source.
$\tilde{S}$ The signal from a measured (unknown) source.
$S_{\rm Kx}$ Linear residual standard deviation of modeled radiance ratios from water-leaving radiance ratios.

$t_f(\lambda)$ Upward Fresnel transmittance through the air-sea interface for radiance.

x Horizontal spatial coordinate.

y Vertical spatial coordinate.

z Depth, in meters, below the air-sea interface.
z_{90} Depth, in meters, equal to the first attenuation length.

δ Relative standard uncertainty.
Δ_L Radiance gradient.

λ Wavelength.

σ Standard deviation.

References

Austin, R.W., and T.J. Petzold, 1981: "The Determination of the Diffuse Attenuation Coefficient of Sea Water Using the Coastal Zone Color Scanner." In: J.F.R. Gower, Ed., *Oceanography from Space,* Plenum Press, New York, 239-256.

Barnes, R.A., W.L. Barnes, W.E. Esaias, and C.R. McClain, 1994a: Prelaunch Acceptance Report for the SeaWiFS Radiometer. *NASA Tech. Memo. 104566, Vol. 22,* S.B. Hooker, E.R. Firestone, and J.G. Acker, Eds., NASA Goddard Space Flight Center, Greenbelt, Maryland, 32 pp.

——, A.W. Holmes, W.L. Barnes, W.E. Esaias, C.R. McClain, and T. Svitek, 1994b: SeaWiFS Prelaunch Radiometric Calibration and Spectral Characterization. *NASA Tech. Memo. 104566, Vol. 23,* S.B. Hooker, E.R. Firestone, and J.G. Acker, Eds., NASA Goddard Space Flight Center, Greenbelt, Maryland, 55 pp.

——, A.W. Holmes, and W.E. Esaias, 1995: Stray Light in the SeaWiFS Radiometer. *NASA Tech. Memo. 104566, Vol. 31,* S.B. Hooker, E.R. Firestone, and J.G. Acker, Eds., NASA Goddard Space Flight Center, Greenbelt, Maryland, 43 pp.

——, E-n. Yeh, and R.E. Eplee, 1996: SeaWiFS Calibration Topics, Part 1. *NASA Tech. Memo. 104566, Vol. 39,* S.B. Hooker and E.R. Firestone, Eds., NASA Goddard Space Flight Center, Greenbelt, Maryland, 18–38.

Hovis, W.A., and J.S. Knoll, 1983: Characteristics of an internally illuminated calibration sphere. *Appl. Opt.,* **22,** 4,004–4,007.

Johnson, B.C., S.S. Bruce, E.A. Early, J.M. Houston, T.R. O'Brian, A. Thompson, S.B. Hooker, and J.L. Mueller, 1996: The Fourth SeaWiFS Intercalibration Round-Robin Experiment (SIRREX-4), May 1995. *NASA Tech. Memo. 104566, Vol. 37,* S.B. Hooker and E.R. Firestone, Eds., NASA Goddard Space Flight Center, Greenbelt, Maryland, 65 pp.

——, J.B. Fowler, and C.L. Cromer, 1997: The SeaWiFS Transfer Radiometer. *SeaWiFS Postlaunch Technical Report Series,* S.B. Hooker and E.R. Firestone, Eds., Greenbelt, Maryland (submitted).

Kostkowski, H.J., and F.E. Nicodemus, 1978: An Introduction to the Measurement Equation. *NBS Tech. Note 910–2, Chapter 5,* F.E. Nicodemus, Ed., U.S. Dept. of Commerce, National Bureau of Standards, Washington, D.C., 58–104.

McClain, C.R., W.E. Esaias, W. Barnes, B. Guenther, D. Endres, S. Hooker, G. Mitchell, and R. Barnes, 1992: Calibration and Validation Plan for SeaWiFS. *NASA Tech. Memo. 104566, Vol. 3,* S.B. Hooker and E.R. Firestone, Eds., NASA Goddard Space Flight Center, Greenbelt, Maryland, 41 pp.

Mielenz, K.D., R.D. Saunders, and J.B. Shumaker, 1990: Spectroradiometric determination of the freezing temperature of gold. *J. Res. Natl. Inst. Stand. Technol.,* **95,** 49–67.

Morel, A., and B. Gentili, 1996: Diffuse reflectance of oceanic waters. III. Implication of bidirectionality for the remote sensing problem. *Appl. Opt.,* **35,** 4,850–4,862.

Mueller, J.L., 1991: Integral Method for Analyzing Irradiance and Radiance Attenuation Profiles. *CHORS Tech. Memo. 007-91,* San Diego State University Center for Hydro-Optics and Remote Sensing, San Diego, California, 10 pp.

——, 1993a: The First SeaWiFS Intercalibration Round-Robin Experiment, SIRREX-1, July 1992. *NASA Tech. Memo. 104566, Vol. 14,* S.B. Hooker and E.R. Firestone, Eds., NASA Goddard Space Flight Center, Greenbelt, Maryland, 60 pp.

——, 1993b: An Optical Climatology of the Northeast Pacific Ocean. *CHORS Tech. Memo. 001-93,* San Diego State University Center for Hydro-Optics and Remote Sensing, San Diego, California, 46 pp. plus appendices.

——, 1995: SeaWiFS Pre-Launch Algorithm for the Diffuse Attenuation Coefficient $K(490)$. *CHORS Tech. Memo. 003-95,* San Diego State University Center for Hydro-Optics and Remote Sensing, San Diego, California, San Diego, California, 11 pp.

——, B.C. Johnson, C.L. Cromer, J.W. Cooper, J.T. McLean, S.B. Hooker, and T.L. Westphal, 1994: The Second SeaWiFS Intercalibration Round-Robin Experiment (SIRREX-2), June 1993. *NASA Tech. Memo. 104566, Vol. 16,* S.B. Hooker and E.R. Firestone, Eds., NASA Goddard Space Flight Center, Greenbelt, Maryland, 121 pp.

——, B.C. Johnson, S.B. Hooker, J.T. McLean, and S. Biggar, 1995: The Third SeaWiFS Intercalibration Round-Robin Experiment (SIRREX-3), 19–30 September 1994. *NASA Tech. Memo. 104566, Vol. 34,* S.B. Hooker, E.R. Firestone, and J.G. Acker, Eds., NASA Goddard Space Flight Center, Greenbelt, Maryland, 78 pp.

Neckel, H., and D. Labs, 1984: The solar radiation between 3300 and 12500 Å. *Solar Phys.,* **90,** 205–258.

Smith, G.R., R.H. Levin, P. Abel, and H. Jacobowitz, 1988: Calibration of the solar channels of the NOAA-9 AVHRR using high altitude aircraft measurements. *J. Atmos. Ocean. Tech.,* **5,** 631–639.

——, ——, R.S. Koyanagi, and R.C. Wrigley, 1989a: Calibration of the Visible and Near-Infrared Channels of the NOAA-9 AVHRR Using High-Altitude Aircraft Measurements from August 1985 and October 1986. *NASA Tech. Memo. 101063,* NASA Ames Research Center, Moffett Field, California, 18 pp.

——, ——, ——, and ——, 1989b: Calibration of the Visible and Near-Infrared Channels of the GOES-6 VISSR Using High-Altitude Aircraft Measurements. *NASA Tech. Memo. 101064,* NASA Ames Research Center, Moffett Field, California, 14 pp.

——, ——, ——, and ——, 1990: Calibration of the Visible and Near-Infrared Channels of the LANDSAT-5 Thematic Mapper Using High-Altitude Aircraft Measurements. *NASA Tech. Memo. 102185,* NASA Ames Research Center, Moffett Field, California, 15 pp.

Walker, J.H., R.D. Saunders, J.K. Jackson, and D.A. McSparron, 1987a: Spectral Irradiance Calibrations. *NBS Special Publication 250–20*, U.S. Dept. of Commerce, National Bureau of Standards, Washington, D.C., 37 pp. plus appendices.

——, ——, and A.T. Hattenburg, 1987b: Spectral Radiance Calibrations. *NBS Special Publication 250–1,* U.S. Dept. of Commerce, National Bureau of Standards, Washington, D.C., 26 pp. plus appendices.

The SeaWiFS Technical Report Series

Vol. 1

Hooker, S.B., W.E. Esaias, G.C. Feldman, W.W. Gregg, and C.R. McClain, 1992: An Overview of SeaWiFS and Ocean Color. *NASA Tech. Memo. 104566, Vol. 1,* S.B. Hooker and E.R. Firestone, Eds., NASA Goddard Space Flight Center, Greenbelt, Maryland, 24 pp., plus color plates.

Vol. 2

Gregg, W.W., 1992: Analysis of Orbit Selection for SeaWiFS: Ascending vs. Descending Node. *NASA Tech. Memo. 104566, Vol. 2,* S.B. Hooker and E.R. Firestone, Eds., NASA Goddard Space Flight Center, Greenbelt, Maryland, 16 pp.

Vol. 3

McClain, C.R., W.E. Esaias, W. Barnes, B. Guenther, D. Endres, S. Hooker, G. Mitchell, and R. Barnes, 1992: Calibration and Validation Plan for SeaWiFS. *NASA Tech. Memo. 104566, Vol. 3,* S.B. Hooker and E.R. Firestone, Eds., NASA Goddard Space Flight Center, Greenbelt, Maryland, 41 pp.

Vol. 4

McClain, C.R., E. Yeh, and G. Fu, 1992: An Analysis of GAC Sampling Algorithms: A Case Study. *NASA Tech. Memo. 104566, Vol. 4,* S.B. Hooker and E.R. Firestone, Eds., NASA Goddard Space Flight Center, Greenbelt, Maryland, 22 pp., plus color plates.

Vol. 5

Mueller, J.L., and R.W. Austin, 1992: Ocean Optics Protocols for SeaWiFS Validation. *NASA Tech. Memo. 104566, Vol. 5,* S.B. Hooker and E.R. Firestone, Eds., NASA Goddard Space Flight Center, Greenbelt, Maryland, 43 pp.

Vol. 6

Firestone, E.R., and S.B. Hooker, 1992: SeaWiFS Technical Report Series Summary Index: Volumes 1–5. *NASA Tech. Memo. 104566, Vol. 6,* S.B. Hooker and E.R. Firestone, Eds., NASA Goddard Space Flight Center, Greenbelt, Maryland, 9 pp.

Vol. 7

Darzi, M., 1992: Cloud Screening for Polar Orbiting Visible and IR Satellite Sensors. *NASA Tech. Memo. 104566, Vol. 7,* S.B. Hooker and E.R. Firestone, Eds., NASA Goddard Space Flight Center, Greenbelt, Maryland, 7 pp.

Vol. 8

Hooker, S.B., W.E. Esaias, and L.A. Rexrode, 1993: Proceedings of the First SeaWiFS Science Team Meeting. *NASA Tech. Memo. 104566, Vol. 8,* S.B. Hooker and E.R. Firestone, Eds., NASA Goddard Space Flight Center, Greenbelt, Maryland, 61 pp.

Vol. 9

Gregg, W.W., F.C. Chen, A.L. Mezaache, J.D. Chen, J.A. Whiting, 1993: The Simulated SeaWiFS Data Set, Version 1. *NASA Tech. Memo. 104566, Vol. 9,* S.B. Hooker, E.R. Firestone, and A.W. Indest, Eds., NASA Goddard Space Flight Center, Greenbelt, Maryland, 17 pp.

Vol. 10

Woodward, R.H., R.A. Barnes, C.R. McClain, W.E. Esaias, W.L. Barnes, and A.T. Mecherikunnel, 1993: Modeling of the SeaWiFS Solar and Lunar Observations. *NASA Tech. Memo. 104566, Vol. 10,* S.B. Hooker and E.R. Firestone, Eds., NASA Goddard Space Flight Center, Greenbelt, Maryland, 26 pp.

Vol. 11

Patt, F.S., C.M. Hoisington, W.W. Gregg, and P.L. Coronado, 1993: Analysis of Selected Orbit Propagation Models for the SeaWiFS Mission. *NASA Tech. Memo. 104566, Vol. 11,* S.B. Hooker, E.R. Firestone, and A.W. Indest, Eds., NASA Goddard Space Flight Center, Greenbelt, Maryland, 16 pp.

Vol. 12

Firestone, E.R., and S.B. Hooker, 1993: SeaWiFS Technical Report Series Summary Index: Volumes 1–11. *NASA Tech. Memo. 104566, Vol. 12,* S.B. Hooker and E.R. Firestone, Eds., NASA Goddard Space Flight Center, Greenbelt, Maryland, 28 pp.

Vol. 13

McClain, C.R., K.R. Arrigo, J. Comiso, R. Fraser, M. Darzi, J.K. Firestone, B. Schieber, E-n. Yeh, and C.W. Sullivan, 1994: Case Studies for SeaWiFS Calibration and Validation, Part 1. *NASA Tech. Memo. 104566, Vol. 13,* S.B. Hooker and E.R. Firestone, Eds., NASA Goddard Space Flight Center, Greenbelt, Maryland, 52 pp., plus color plates.

Vol. 14

Mueller, J.L., 1993: The First SeaWiFS Intercalibration Round-Robin Experiment, SIRREX-1, July 1992. *NASA Tech. Memo. 104566, Vol. 14,* S.B. Hooker and E.R. Firestone, Eds., NASA Goddard Space Flight Center, Greenbelt, Maryland, 60 pp.

Vol. 15

Gregg, W.W., F.S. Patt, and R.H. Woodward, 1994: The Simulated SeaWiFS Data Set, Version 2. *NASA Tech. Memo. 104566, Vol. 15,* S.B. Hooker and E.R. Firestone, Eds., NASA Goddard Space Flight Center, Greenbelt, Maryland, 42 pp., plus color plates.

Vol. 16

Mueller, J.L., B.C. Johnson, C.L. Cromer, J.W. Cooper, J.T. McLean, S.B. Hooker, and T.L. Westphal, 1994: The Second SeaWiFS Intercalibration Round-Robin Experiment, SIRREX-2, June 1993. *NASA Tech. Memo. 104566, Vol. 16,* S.B. Hooker and E.R. Firestone, Eds., NASA Goddard Space Flight Center, Greenbelt, Maryland, 121 pp.

Vol. 17

Abbott, M.R., O.B. Brown, H.R. Gordon, K.L. Carder, R.E. Evans, F.E. Muller-Karger, and W.E. Esaias, 1994: Ocean Color in the 21st Century: A Strategy for a 20-Year Time Series. *NASA Tech. Memo. 104566, Vol. 17,* S.B. Hooker and E.R. Firestone, Eds., NASA Goddard Space Flight Center, Greenbelt, Maryland, 20 pp.

Vol. 18

Firestone, E.R., and S.B. Hooker, 1994: SeaWiFS Technical Report Series Summary Index: Volumes 1–17. *NASA Tech. Memo. 104566, Vol. 18,* S.B. Hooker and E.R. Firestone, Eds., NASA Goddard Space Flight Center, Greenbelt, Maryland, 47 pp.

Vol. 19

McClain, C.R., R.S. Fraser, J.T. McLean, M. Darzi, J.K. Firestone, F.S. Patt, B.D. Schieber, R.H. Woodward, E-n. Yeh, S. Mattoo, S.F. Biggar, P.N. Slater, K.J. Thome, A.W. Holmes, R.A. Barnes, and K.J. Voss, 1994: Case Studies for SeaWiFS Calibration and Validation, Part 2. *NASA Tech. Memo. 104566, Vol. 19,* S.B. Hooker, E.R. Firestone, and J.G. Acker, Eds., NASA Goddard Space Flight Center, Greenbelt, Maryland, 73 pp.

Vol. 20

Hooker, S.B., C.R. McClain, J.K. Firestone, T.L. Westphal, E-n. Yeh, and Y. Ge, 1994: The SeaWiFS Bio-Optical Archive and Storage System (SeaBASS), Part 1. *NASA Tech. Memo. 104566, Vol. 20,* S.B. Hooker and E.R. Firestone, Eds., NASA Goddard Space Flight Center, Greenbelt, Maryland, 40 pp.

Vol. 21

Acker, J.G., 1994: The Heritage of SeaWiFS: A Retrospective on the CZCS NIMBUS Experiment Team (NET) Program. *NASA Tech. Memo. 104566, Vol. 21,* S.B. Hooker and E.R. Firestone, Eds., NASA Goddard Space Flight Center, Greenbelt, Maryland, 43 pp.

Vol. 22

Barnes, R.A., W.L. Barnes, W.E. Esaias, and C.R. McClain, 1994: Prelaunch Acceptance Report for the SeaWiFS Radiometer. *NASA Tech. Memo. 104566, Vol. 22,* S.B. Hooker, E.R. Firestone, and J.G. Acker, Eds., NASA Goddard Space Flight Center, Greenbelt, Maryland, 32 pp.

Vol. 23

Barnes, R.A., A.W. Holmes, W.L. Barnes, W.E. Esaias, C.R. McClain, and T. Svitek, 1994: SeaWiFS Prelaunch Radiometric Calibration and Spectral Characterization. *NASA Tech. Memo. 104566, Vol. 23,* S.B. Hooker, E.R. Firestone, and J.G. Acker, Eds., NASA Goddard Space Flight Center, Greenbelt, Maryland, 55 pp.

Vol. 24

Firestone, E.R., and S.B. Hooker, 1995: SeaWiFS Technical Report Series Summary Index: Volumes 1–23. *NASA Tech. Memo. 104566, Vol. 24,* S.B. Hooker and E.R. Firestone, Eds., NASA Goddard Space Flight Center, Greenbelt, Maryland, 36 pp.

Vol. 25

Mueller, J.L., and R.W. Austin, 1995: Ocean Optics Protocols for SeaWiFS Validation, Revision 1. *NASA Tech. Memo. 104566, Vol. 25,* S.B. Hooker and E.R. Firestone, Eds., NASA Goddard Space Flight Center, Greenbelt, Maryland, 67 pp.

Vol. 26

Siegel, D.A., M.C. O'Brien, J.C. Sorensen, D.A. Konnoff, E.A. Brody, J.L. Mueller, C.O. Davis, W.J. Rhea, and S.B. Hooker, 1995: Results of the SeaWiFS Data Analysis Round-Robin (DARR), July 1994. *NASA Tech. Memo. 104566, Vol. 26,* S.B. Hooker and E.R. Firestone, Eds., NASA Goddard Space Flight Center, Greenbelt, Maryland, 58 pp.

Vol. 27

Mueller, J.L., R.S. Fraser, S.F. Biggar, K.J. Thome, P.N. Slater, A.W. Holmes, R.A. Barnes, C.T. Weir, D.A. Siegel, D.W. Menzies, A.F. Michaels, and G. Podesta 1995: Case Studies for SeaWiFS Calibration and Validation, Part 3. *NASA Tech. Memo. 104566, Vol. 27,* S.B. Hooker, E.R. Firestone, and J.G. Acker, Eds., NASA Goddard Space Flight Center, Greenbelt, Maryland, 46 pp.

Vol. 28

McClain, C.R., K.R. Arrigo, W.E. Esaias, M. Darzi, F.S. Patt, R.H. Evans, J.W. Brown, C.W. Brown, R.A. Barnes, and L. Kumar, 1995: SeaWiFS Algorithms, Part 1. *NASA Tech. Memo. 104566, Vol. 28,* S.B. Hooker, E.R. Firestone, and J.G. Acker, Eds., NASA Goddard Space Flight Center, Greenbelt, Maryland, 38 pp., plus color plates.

Vol. 29

Aiken, J., G.F. Moore, C.C. Trees, S.B. Hooker, and D.K. Clark, 1995: The SeaWiFS CZCS-Type Pigment Algorithm. *NASA Tech. Memo. 104566, Vol. 29,* S.B. Hooker and E.R. Firestone, Eds., NASA Goddard Space Flight Center, Greenbelt, Maryland, 34 pp.

Vol. 30

Firestone, E.R., and S.B. Hooker, 1996: SeaWiFS Technical Report Series Cumulative Index: Volumes 1–29. *NASA Tech. Memo. 104566, Vol. 30,* S.B. Hooker and E.R. Firestone, Eds., NASA Goddard Space Flight Center, Greenbelt, Maryland, 43 pp.

Vol. 31

Barnes, R.A., A.W. Holmes, and W.E. Esaias, 1995: Stray Light in the SeaWiFS Radiometer. *NASA Tech. Memo. 104566, Vol. 31,* S.B. Hooker, E.R. Firestone, and J.G. Acker, Eds., NASA Goddard Space Flight Center, Greenbelt, Maryland, 76 pp.

Vol. 32

Campbell, J.W., J.M. Blaisdell, and M. Darzi, 1995: Level-3 SeaWiFS Data Products: Spatial and Temporal Binning Algorithms. *NASA Tech. Memo. 104566, Vol. 32,* S.B. Hooker, E.R. Firestone, and J.G. Acker, Eds., NASA Goddard Space Flight Center, Greenbelt, Maryland, 73 pp., plus color plates.

Vol. 33

Moore, G.F., and S.B. Hooker, 1996: Proceedings of the First SeaWiFS Exploitation Initiative (SEI) Team Meeting. *NASA Tech. Memo. 104566, Vol. 33,* S.B. Hooker and E.R. Firestone, Eds., NASA Goddard Space Flight Center, Greenbelt, Maryland, 53 pp.

Vol. 34

Mueller, J.L., B.C. Johnson, C.L. Cromer, S.B. Hooker, J.T. McLean, and S.F. Biggar, 1996: The Third SeaWiFS Intercalibration Round-Robin Experiment (SIRREX-3), 19–30 September 1994. *NASA Tech. Memo. 104566, Vol. 34,* S.B. Hooker, E.R. Firestone, and J.G. Acker, Eds., NASA Goddard Space Flight Center, Greenbelt, Maryland, 78 pp.

Vol. 35

Robins, D.B., A.J. Bale, G.F. Moore, N.W. Rees, S.B. Hooker, C.P. Gallienne, A.G. Westbrook, E. Marañón, W.H. Spooner, and S.R. Laney, 1996: AMT-1 Cruise Report and Preliminary Results. *NASA Tech. Memo. 104566, Vol. 35,* S.B. Hooker and E.R. Firestone, Eds., NASA Goddard Space Flight Center, Greenbelt, Maryland, 87 pp.

Vol. 36

Firestone, E.R., and S.B. Hooker, 1996: SeaWiFS Technical Report Series Cumulative Index: Volumes 1–35. *NASA Tech. Memo. 104566, Vol. 36,* S.B. Hooker and E.R. Firestone, Eds., NASA Goddard Space Flight Center, Greenbelt, Maryland, 55 pp.

Vol. 37

Johnson, B.C., S.S. Bruce, E.A. Early, J.M. Houston, T.R. O'Brian, A. Thompson, S.B. Hooker, and J.L. Mueller, 1996: The Fourth SeaWiFS Intercalibration Round-Robin Experiment (SIRREX-4), May 1995. *NASA Tech. Memo. 104566, Vol. 37,* S.B. Hooker and E.R. Firestone, Eds., NASA Goddard Space Flight Center, Greenbelt, Maryland, 65 pp.

Vol. 38

McClain, C.R., M. Darzi, R.A. Barnes, R.E. Eplee, J.K. Firestone, F.S. Patt, W.D. Robinson, B.D. Schieber, R.H. Woodward, and E-n. Yeh, 1996: SeaWiFS Calibration and Validation Quality Control Procedures. *NASA Tech. Memo. 104566, Vol. 38,* S.B. Hooker and E.R. Firestone, Eds., NASA Goddard Space Flight Center, Greenbelt, Maryland, 68 pp.

Vol. 39

Barnes, R.A., E-n. Yeh, and R.E. Eplee, 1996: SeaWiFS Calibration Topics, Part 1. *NASA Tech. Memo. 104566, Vol. 39,* S.B. Hooker and E.R. Firestone, Eds., NASA Goddard Space Flight Center, Greenbelt, Maryland, 66 pp.

Vol. 40

Barnes, R.A., R.E. Eplee, Jr., E-n. Yeh, and W.E. Esaias, 1997: SeaWiFS Calibration Topics, Part 2. *NASA Tech. Memo. 104566, Vol. 40,* S.B. Hooker and E.R. Firestone, Eds., NASA Goddard Space Flight Center, Greenbelt, Maryland, 67 pp.

Vol. 41

Yeh, E-n., R.A. Barnes, M. Darzi, L. Kumar, E.A. Early, B.C. Johnson, and J.L. Mueller, 1997: Case Studies for SeaWiFS Calibration and Validation, Part 4. *NASA Tech. Memo. 104566, Vol. 41,* S.B. Hooker and E.R. Firestone, Eds., NASA Goddard Space Flight Center, Greenbelt, Maryland, 35 pp.

REPORT DOCUMENTATION PAGE

Form Approved
OMB No. 0704-0188

1. AGENCY USE ONLY *(Leave blank)*	2. REPORT DATE	3. REPORT TYPE AND DATES COVERED
	August 1997	Technical Memorandum

4. TITLE AND SUBTITLE
SeaWiFS Technical Report Series
Volume 41: Case Studies for SeaWiFS Calibration and Validation, Part 4

5. FUNDING NUMBERS
Code 970.2

6. AUTHOR(S)
Eueng-nan Yeh, Robert A. Barnes, Michael Darzi, Lakshmi Kumar, Edward A. Early, B. Carol Johnson, James L. Mueller, and Charles C. Trees
Series Editors: Stanford B. Hooker and Elaine R. Firestone

7. PERFORMING ORGANIZATION NAME(S) AND ADDRESS(ES)
Laboratory for Hydrospheric Processes
Goddard Space Flight Center
Greenbelt, Maryland 20771

8. PERFORMING ORGANIZATION REPORT NUMBER
97B00080

9. SPONSORING/MONITORING AGENCY NAME(S) AND ADDRESS(ES)
National Aeronautics and Space Administration
Washington, D.C. 20546–0001

10. SPONSORING/MONITORING AGENCY REPORT NUMBER
TM–104566, Vol. 41

11. SUPPLEMENTARY NOTES
Elaine R. Firestone, Eueng-nan Yeh, Robert A. Barnes, and Michael Darzi: General Sciences Corporation, Laurel, Maryland; Lakshmi Kumar: Hughes STX, Landover, Maryland; Edward A. Early and B. Carol Johnson: National Institute of Standards and Technology, Gaithersburg, Maryland; and James L. Mueller and Charles C. Trees: Center for Hydro-Optics and Remote Sensing, San Diego State University, San Diego, California

12a. DISTRIBUTION/AVAILABILITY STATEMENT
Unclassified–Unlimited
Subject Category 48
Report is available from the Center for AeroSpace Information (CASI), 7121 Standard Drive, Hanover, MD 21076–1320; (301)621-0390

12b. DISTRIBUTION CODE

13. ABSTRACT *(Maximum 200 words)*

This document provides brief reports, or case studies, on a number of investigations sponsored by the Calibration and Validation Team (CVT) within the Sea-viewing Wide Field-of-view Sensor (SeaWiFS) Project. Chapter 1 describes the calibration and characterization of the GSFC sphere, which was used in the recent recalibration of the SeaWiFS instrument. Chapter 2 presents a revision of the diffuse attenuation coefficient, K(490), algorithm based on the SeaWiFS wavelengths. Chapter 3 provides an implementation scheme for an algorithm to remove out-of-band radiance when using a sensor calibration based on a finite width (truncated) spectral response function, e.g., between the 1% transmission points. Chapter 4 describes the implementation schemes for the stray light quality flag (local area coverage [LAC] and global area coverage [GAC]) and the LAC stray light correction.

14. SUBJECT TERMS
SeaWiFS, Oceanography, Calibration, Validation, Case Studies, GSFC Sphere, Diffuse Attenuation Coefficient, K(490), Out-of-Band Correction Algorithm, Stray Light Correction Algorithm

15. NUMBER OF PAGES
35

16. PRICE CODE

17. SECURITY CLASSIFICATION OF REPORT	18. SECURITY CLASSIFICATION OF THIS PAGE	19. SECURITY CLASSIFICATION OF ABSTRACT	20. LIMITATION OF ABSTRACT
Unclassified	Unclassified	Unclassified	Unlimited